



## Research paper

# A nonlinear 3D model for iron-based shape memory alloys considering different thermomechanical properties for austenite and martensite and coupling between transformation and plasticity



Cheikh Cissé<sup>a</sup>, Wael Zaki<sup>a,\*</sup>, Xiaojun Gu<sup>b</sup>, Tarak Ben Zineb<sup>a,c,d</sup>

<sup>a</sup> Khalifa University of Science, Technology, and Research, P.O. Box 127788, Abu Dhabi, UAE

<sup>b</sup> Northwestern Polytechnical University, 127 Youyi West Rd, Xi'an, Shaanxi 710072, China

<sup>c</sup> Université de Lorraine, LEMTA, UMR 7563, Vandoeuvre-lès-Nancy F-54500, France

<sup>d</sup> CNRS, LEMTA, UMR 7563, Vandoeuvre-lès-Nancy F-54500, France

## ARTICLE INFO

## Article history:

Received 9 December 2015

Revised 11 January 2017

Available online 1 February 2017

## Keywords:

Iron-based shape memory alloys

Phenomenological model

Shape memory effect

Cyclic phase transformation

Monolithic and reversed plasticity

## ABSTRACT

The paper presents a 3D macroscopic constitutive model for Iron-based shape memory alloys (Fe-SMAs) that uses different thermomechanical properties for austenite and martensite, and considers nonlinear coupling effects between phase transformation and plasticity. The constitutive equations are derived from a potential comprising the Voigt mixture of the free energies of the two phases adapted from the ZM model, and a new interaction energy term. The loading conditions for phase transformation and plastic deformation are obtained by requiring the governing thermodynamic forces to derive from an appropriate dissipation potential, in which a quadratic plasticity-dependent term has been introduced to account for its suppressive effect on forward transformation. The model is implemented in ABAQUS through a user defined material subroutine (UMAT), validated against experimental data taken from the literature, and used to simulate partial unloading and investigate the influences of interaction parameters. Finite element analysis of a precracked compact tension sample is then carried out under both plane stress and plane strain (nonproportional stress fields with strong gradients). The results show highly heterogeneous stress distribution in the specimen. The inelastic strain singularity at the crack front is a consequence of pure phase transformation at low temperature, pure plasticity at high temperature, and a mix of both at intermediate temperatures. During unloading, the crack front accommodates the compression of the surrounding material by undergoing cyclic phase transformation and/or reversed plasticity, which, in turn, induces partial crack closure. If the mechanical loading cycle is operated at low temperature then heating leads to complete crack closure due to martensite → austenite transformation, while if it is operated at elevated temperature, heating leads to further but not complete crack closure as a result of the thermal-induced plasticity.

© 2017 Elsevier Ltd. All rights reserved.

## 1. Introduction

Shape memory alloys (SMAs) can experience severe inelastic deformation that can be recovered by heating or unloading, depending on prior loading history. The origin of this unusual behavior is a first-order, solid-solid, diffusionless and reversible phase change called martensitic transformation, which takes place between a parent austenite phase (A) and a product martensite phase (M) (Chang and Read, 1951; Buehler et al., 1963; Olson and Cohen, 1982). Shape recovery can be accomplished by heating,

giving rise to a “shape memory” effect (SME), or by mechanical unloading resulting in a pseudoelastic behavior (PE). The shape memory effect, in particular, was first reported by Chang and Read (1951) in a Au–Cd alloy. It was later observed in many NiTi, Cu, and Fe alloys, which are collectively the most used SMAs today. A general and detailed overview of shape memory alloys can be found in Cissé et al. (2016a) and Cissé et al. (2016b).

Compared to Cu-based and Fe-based SMAs, Nitinol is biocompatible (Buehler and Cross, 1969; Shabalovskaya, 1996; Es-Souni et al., 2005; Bansiddhi et al., 2008) and shows higher corrosion resistance and more pronounced dependence of the thermomechanical behavior on loading rate (Araya et al., 2008; Araki et al., 2012), grain size (Sutou et al., 2013) and temperature (Sutou et al., 2009; Niitsu et al., 2011). In contrast, polycrystalline Cu-based SMAs are

\* Corresponding author.

E-mail addresses: [cheikh.cisse@kustar.ac.ae](mailto:cheikh.cisse@kustar.ac.ae) (C. Cissé), [wael.zaki@kustar.ac.ae](mailto:wael.zaki@kustar.ac.ae) (W. Zaki), [gu.xiaojun@live.cn](mailto:gu.xiaojun@live.cn) (X. Gu), [tarak.ben-zineb@univ-lorraine.fr](mailto:tarak.ben-zineb@univ-lorraine.fr) (T. Ben Zineb).

brittle and therefore challenging to use in engineering applications (Casciati et al., 2007; Ueland and Schuh, 2012). Both alloys show high achievable strain recovery (Otsuka and Wayman, 1999; Miyazaki et al., 1999; Johnson, 2013) as well as narrow thermal hysteresis, elevated cost, and low weldability and machinability (Jalaeefer and Asgarian, 2013). Moreover, NiTi appears to be comparable to polycrystalline CuAlBe (Siredey et al., 2005) and oligocrystalline CuZnAl SMAs (Ueland and Schuh, 2012), but superior to single crystal and polycrystalline CuZnAl in terms of fatigue endurance, based on the results of rotary bending tests reported by Miyazaki et al. (1999) and Vincent et al. (2015). Fe-based SMAs, on the other hand, were first investigated by Sato et al. (1982) and found to exhibit larger hysteresis, higher elastic stiffness and ductility, and lower shape recovery (about 4%) compared to NiTi and Cu-based alloys (Cladera et al., 2014). They also offer lower cost and better workability, weldability and machinability (Kajiwara, 1999), which make them attractive for larger and more complex engineering structures. Yamauchi et al. (2011) distinguished two main categories of Fe-SMAs: The first category comprises Fe-Pt, Fe-Pd and Fe-Ni-Co alloys that display thermoelastic phase transformation, similar to NiTi and Cu-based SMAs, with small thermal hysteresis and high SME (up to 13%) (Tanaka et al., 2010), while the second category includes Fe-Ni-C and Fe-Mn-Si alloys, characterized by nonthermoelastic transformation accompanied with large thermal hysteresis and moderate SME ranging from 2.5% without training to 4% for trained material. This low SME in Fe-Mn-Si alloys can be improved by training (Federzoni et al., 1993; Wang et al., 1995; Zhao, 1999), precipitation (Rong et al., 1995; Kajiwara et al., 2001; Stanford et al., 2008; Wen et al., 2008), heat treatment and rolling (Stanford and Dunne, 2006; Baruj and Troiani, 2008; Druker et al., 2011) as well as a combination of aging, pre-straining and training (Lin et al., 2014).

Phase transformation in NiTi occurs by homogeneous shearing of the body-centered cubic (BCC) austenite lattice into a hexagonal close-packed (HCP) martensite lattice. In the case of Fe-Mn-Si, the HCP martensitic phase is formed by slippage of the face-centered cubic (FCC) austenitic microstructure. This mechanism is based on Shockley dislocation during which the three-plane stacking sequence (ABC) of FCC changes to a two-plane sequence of type (ABA). Due to this change, the slippage does not preclude reverse transformation, in contrast to plasticity where the initial and final microstructure have the same crystal lattices despite the rearrangement of atoms (Cladera et al., 2014). In addition, Fe-Mn-Si displays higher ductility compared to NiTi, and a yield strength that decreases noticeably with increasing temperature (Khalil et al., 2013). The increased ductility is due to facilitated slippage on closely packed atomic planes, which have a higher packing factor in FCC than in BCC crystals. With regard to the influence of material composition, Otsuka (1991) found that adding up to 7% (wt%) Cr improves the corrosion resistance of Fe-Mn-Si alloys. The author also observed that high Mn concentration stabilizes the austenitic phase whereas a low Mn concentration promotes the formation of irreversible body-centered tetragonal (BCT) martensite. This loss of SME due to lower Mn content can be countered by increasing Si concentration (Sato et al., 1982). Recently, Peng et al. (2015) found that SME in Fe-SMAs can also be improved by the addition of carbon after thermomechanical treatment.

In Fe-Mn-Si crystals, twelve martensite variants can be formed in four habit planes along three directions (Cladera et al., 2014). However, the energy gap between these variants is very high compared to the plastic gliding energy (Goluboroda et al., 1999), which makes reorientation of pre-existing martensite variants virtually impossible. For this reason, the inelastic deformation in Fe-Mn-Si is mostly due to plastic slip or to stress-induced martensite transformation in the temperature range  $[M_s^0, A_s^0]$ , where  $M_s^0$  and  $A_s^0$  are,

respectively, the martensite start and austenite start temperatures at zero stress.

The current deficiencies in the engineering applications of Fe-SMAs are rooted in the lack of suitable numerical models. Indeed, recent experimental efforts have confirmed the appropriateness of these alloys for large engineering structures such as smart composites (Watanabe et al., 2007) or reinforced concrete beams (Sawaguchi et al., 2006). However, without simulation tools, understanding and predicting the behavior of such structures may be complicated and expensive. Contrary to NiTi and Cu-based SMAs, very few constitutive models are available for Fe-SMAs, with most still limited to uniaxial formulations and/or simulations (Nishimura et al., 1997; Goluboroda et al., 1999; Nishimura et al., 2003; Lazghab and Wu, 2005; Cissé et al., 2015). Nishimura et al. (1997) derived a uniaxial phenomenological model for polycrystalline Fe-SMAs using an exponential flow rule for phase transformation. Goluboroda et al. (1999) proposed a nonlinear unidirectional model for the thermomechanical behavior of Fe-based SMAs considering transformation-dependent yield strength. The model was shown to properly describe the accumulation of inelastic strain during cyclic loading and the nonlinear stress-strain behavior of the SMA near the onset of phase transformation. Later, Lazghab and Wu (2005) developed a uniaxial model that can simulate the shape memory effect and pseudoelasticity of Fe-SMAs in tension and compression, considering the influence of plastic deformation on phase transformation. Jemal et al. (2009) proposed one of the first 3D model for Fe-SMAs, in which the state equations derive from the expression of a Gibbs free energy density. The model considers linear hardening during inelastic deformation, which is not consistent with experimental observations. This shortcoming was addressed by Khalil et al. (2012) through the introduction of nonlinear hardening terms, which allowed better agreement with experimental data at low loading temperatures. The model was implemented in Abaqus for structure analysis, but presents impairments such as quasi-linear plastic hardening, and notable deviation in the stress-strain loading curve and poor prediction of the shape recovery when coupling between transformation and plasticity occurs. A more recent attempt was made by Evard et al. (2016) who proposed a microstructural model for FeMn-based shape memory alloys. However, several restrictions such as linear hardening, the lack of experimental validation and the absence of 3D simulations were reported; thus raising doubts about the capability of their model to properly design Fe-SMA devices. In this context of insufficient representation of Fe-SMAs, a new nonlinear 3D model is proposed in this manuscript. The free energy of the two phases is derived by adapting the approach used in the ZM model (Zaki and Mousni, 2007) to FeMnSi alloys. A new expression of the interaction energy, which is the most important part in any constitutive model, is proposed to account for the directions of the inelastic strains. The pseudo-potential of dissipation is expressed with different thermomechanical properties and considers the plasticity-dependence of the critical force of forward transformation. The paper is organized as follows:

- **Section 2** is dedicated to the derivation of the constitutive equations of the model. This is accomplished by first constructing an expression of the Helmholtz free energy density for Fe-SMAs, which is then augmented to account for constraints on the state variables using the theory of Lagrange multipliers. The resulting Lagrangian, considered as a thermodynamic potential, allows the derivation of the thermodynamic forces used to define the loading conditions for phase transformation and plastic deformation,
- **Section 3** presents the time-discrete integration of the constitutive model,

**Table 1**  
Summary of the constitutive equations.

<p>• <b>Loading functions</b></p> $\mathcal{F}_m^{\text{tr}} = \frac{G_{\text{ma}}}{6} \sigma_{\text{eq}}^2 + \frac{K_{\text{ma}}}{2} \sigma_{\text{h}}^2 + \sigma : (\bar{\epsilon}_{\text{tr}} - \bar{\epsilon}_{\text{pl}}) - \zeta_m (T - M_s^0) - H_v (\bar{\epsilon}_{\text{tr}} : \bar{\epsilon}^{\text{tr}}) (\bar{\epsilon}^{\text{tr}} : \bar{\epsilon}^{\text{tr}})^{\frac{n_p-1}{2}}$ $- H_{pv} \delta_{pv} (\bar{\epsilon}_{\text{tr}} : \bar{\epsilon}^{\text{pl}}) [(\bar{\epsilon}^{\text{tr}} : \bar{\epsilon}^{\text{pl}}) \delta_{pv}]^{n_{pv}} - \sigma_m^{\text{tr}} \epsilon_L - H_s p^2 + (\lambda_1 - \lambda_2),$ $\mathcal{F}_a^{\text{tr}} = -\frac{G_{\text{ma}}}{6} \sigma_{\text{eq}}^2 - \frac{K_{\text{ma}}}{2} \sigma_{\text{h}}^2 - \sigma : (\bar{\epsilon}_{\text{tr}} - \bar{\epsilon}_{\text{pl}}) + \zeta_a (T - A_s^0) + H_v (\bar{\epsilon}_{\text{tr}} : \bar{\epsilon}^{\text{tr}}) (\bar{\epsilon}^{\text{tr}} : \bar{\epsilon}^{\text{tr}})^{\frac{n_p-1}{2}}$ $+ H_{pv} \delta_{pv} (\bar{\epsilon}_{\text{tr}} : \bar{\epsilon}^{\text{pl}}) [(\bar{\epsilon}^{\text{tr}} : \bar{\epsilon}^{\text{pl}}) \delta_{pv}]^{n_{pv}} - \sigma_a^{\text{tr}} \epsilon_L + H_x \xi - (\lambda_1 - \lambda_2),$ $\mathcal{F}_a^{\text{pl}} = (1 - \xi) \left[ \sigma - H_p (\bar{\epsilon}^{\text{pl}} : \bar{\epsilon}^{\text{pl}})^{\frac{n_p-1}{2}} \bar{\epsilon}^{\text{pl}} - H_{pv} \delta_{pv} [(\bar{\epsilon}^{\text{tr}} : \bar{\epsilon}^{\text{pl}}) \delta_{pv}]^{n_{pv}} \bar{\epsilon}^{\text{tr}} \right] : \mathbf{N}^{\text{pl}} - < \sigma_a^{\text{pl}} - \beta T >.$ <p>• <b>Kuhn–Tucker conditions on the loading functions</b></p> $\mathcal{F}_m^{\text{tr}} \leq 0, \quad \dot{\xi} \geq 0, \quad \dot{\xi} \mathcal{F}_m^{\text{tr}} = 0,$ $\mathcal{F}_a^{\text{tr}} \leq 0, \quad -\dot{\xi} \geq 0, \quad (-\dot{\xi}) \mathcal{F}_a^{\text{tr}} = 0,$ $\mathcal{F}_a^{\text{pl}} \leq 0, \quad \dot{p} \geq 0, \quad \dot{p} \mathcal{F}_a^{\text{pl}} = 0.$ <p>• <b>Kuhn–Tucker conditions on the state variables</b></p> $\lambda_1 \geq 0, \quad \lambda_1 \xi = 0,$ $\lambda_2 \geq 0, \quad \lambda_2 (1 - \xi) = 0.$ <p>• <b>Flow rules</b></p> $\bar{\epsilon}^{\text{tr}} = \dot{\xi} \epsilon_L \mathbf{N}^{\text{tr}}, \quad \text{with } \mathbf{N}^{\text{tr}} = \begin{cases} \frac{3}{2} \frac{\mathbf{V}_{\text{tr}}^{\text{dev}}}{V_{\text{tr}}^{\text{tr}}}, & \text{if } \dot{\xi} > 0, \\ \frac{\bar{\epsilon}^{\text{tr}}}{\xi}, & \text{if } \dot{\xi} < 0, \end{cases}$ $\bar{\epsilon}^{\text{pl}} = (1 - \xi) \dot{p} \mathbf{N}^{\text{pl}}, \quad \text{with } \mathbf{N}^{\text{pl}} = \begin{cases} \frac{3}{2} \frac{\mathbf{V}_{\text{pl}}^{\text{dev}}}{V_{\text{pl}}^{\text{pl}}}, & \text{if } \sigma_{\text{eq}} \neq 0, \\ \frac{\bar{\epsilon}^{\text{pl}}}{\epsilon_{\text{pl}}^{\text{eq}}}, & \text{otherwise.} \end{cases}$ <p>• <b>Stress-strain relation</b></p> $\sigma = [(1 - \xi) \mathbf{K}_a^{-1} + \xi \mathbf{K}_m^{-1}]^{-1} : (\bar{\epsilon} - \bar{\epsilon}^{\text{tr}} - \bar{\epsilon}^{\text{pl}}).$
--

- Section 4 provides a detailed procedure for calibrating the parameters of the model from uniaxial tensile tests. The procedure is applied to determine the material parameters corresponding to the experimental results of Khalil et al. (2012).
- In Section 5, the model is first confronted to experimental and numerical data reported in Khalil et al. (2012) and further numerical investigations are made afterward.
- In Section 6, the model is used to predict the thermomechanical response of a precracked compact tension sample at different loading temperatures for both plane stress and plane strain conditions. Important observations relevant to crack closure and thermal-induced plasticity are discussed.

## 2. Derivation of the constitutive relations

The model is developed in a way that is highly imitative of the framework of generalized standard materials (Frémond, 2002; Halphen and Nguyen, 1974), taking into account the presence of constraints on the state variables (Moumni et al., 2008). Due to the very high yield strength of martensite in Fe-Mn-Si alloys, plastic deformation is assumed to take place exclusively in austenite. A possible reason is that plastic gliding is easier in cubic lattice structures such as FCC austenite because of their high symmetry, which gives more closely packed planes in several directions compared to non-cubic lattices like HCP martensite. Therefore, the dissipative processes considered by the model are the stress-induced martensite transformation and the plastic deformation in austenite. The complete set of state variables used to derive the model consists of the following:

- The total strain tensor  $\bar{\epsilon}$ ,
- The temperature  $T$ ,
- The local strain tensors  $\bar{\epsilon}_a$  for austenite and  $\bar{\epsilon}_m$  for martensite,
- The volume fraction of martensite  $\xi$ ,
- The local transformation strain tensor  $\bar{\epsilon}_{\text{tr}}$ ,
- The macroscopic transformation strain tensor  $\bar{\epsilon}^{\text{tr}}$ ,
- The magnitude of cumulated plastic strain  $p$ .

- The average plastic strain tensor of austenite  $\bar{\epsilon}_{\text{pl}}$ ,
- The macroscopic plastic strain tensor  $\bar{\epsilon}^{\text{pl}}$ .

### 2.1. Free energy density

The Helmholtz free energy density  $\Phi$  of the SMA is obtained from those of austenite,  $\Phi_a$ , and martensite,  $\Phi_m$ , by means of a Voigt rule of mixture rule and the incorporation of an interaction energy  $\Phi_{\text{int}}$  so that

$$\Phi = (1 - \xi) \Phi_a + \xi \Phi_a + \Phi_{\text{int}}. \quad (1)$$

The experimental results of Khalil et al. (2012) point out different elastic loading and unloading slopes. This suggests the necessity to use, contrary to existing Fe-SMA models, different elastic moduli for the parent and product phases. From the assumption that plasticity occurs only in austenite, and following Zaki and Moumni (2007) and subsequent developments in Zaki et al. (2011, 2010), Zaki (2010) and Ould Moussa et al. (2012), the free energy density of austenite,  $\Phi_a$ , is taken as

$$\Phi_a = \frac{1}{2} (\bar{\epsilon}_a - \bar{\epsilon}_{\text{pl}}) : \mathbf{K}_a : (\bar{\epsilon}_a - \bar{\epsilon}_{\text{pl}}), \quad (2)$$

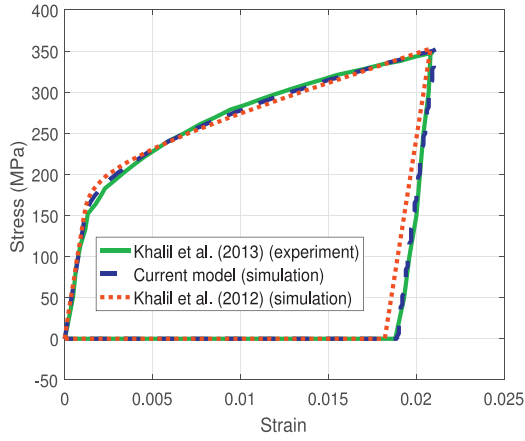
where  $\mathbf{K}_a$  is the elastic stiffness tensor of austenite. The free energy of martensite,  $\Phi_m$ , is given by

$$\Phi_m = \frac{1}{2} (\bar{\epsilon}_m - \bar{\epsilon}_{\text{tr}}) : \mathbf{K}_m : (\bar{\epsilon}_m - \bar{\epsilon}_{\text{tr}}) + C(T), \quad (3)$$

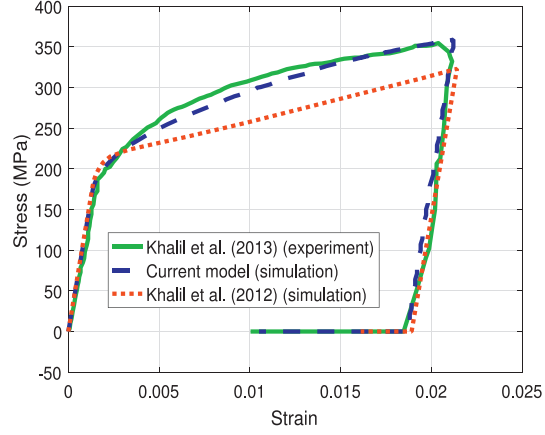
where  $\mathbf{K}_m$  is the elastic stiffness tensor of martensite and  $C(T)$  is a chemical energy density for phase transformation that varies linearly with temperature  $T$  as follows,

$$C(T) = \zeta (T - T_0), \quad (4)$$

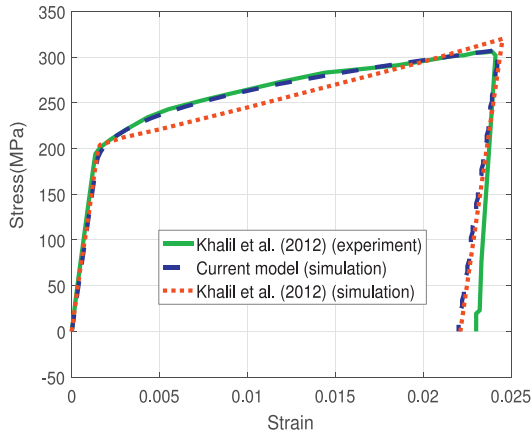
where  $T_0$  is the equilibrium temperature of the alloy and  $\zeta$  is a parameter controlling the influence of temperature on the transformation stress. The experimental work of Nishimura et al. (1999) shows that, in Fe-Mn-Si SMAs, the martensite start line and austenite start line have different slopes. To account for this aspect that was ignored in existing models, the present work considers different values of  $\zeta$  for forward transformation ( $\zeta_m$ ) and reverse phase change ( $\zeta_a$ ). In addition, the following new expression of the



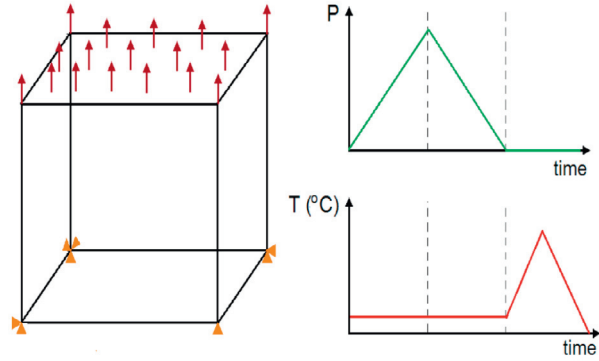
(a) stress-strain behavior at T=20 °C.



(b) stress-strain behavior at T=50 °C.



(c) stress-strain behavior at T=130 °C.



(d) Thermomechanical loading path for the validation.

**Fig. 1.** Experimental and simulated stress-strain curves at  $T = 20, 50$  and  $130$  °C.

interaction energy  $\Phi_{\text{int}}$  where the orientation of the existing elastic strains is accounted for is proposed:

$$\Phi_{\text{int}} = \frac{H_v}{(n_v + 1)} (\mathbf{e}^{\text{tr}} : \mathbf{e}^{\text{tr}})^{\frac{n_v+1}{2}} + \frac{H_p}{(n_p + 1)} (\mathbf{e}^{\text{pl}} : \mathbf{e}^{\text{pl}})^{\frac{n_p+1}{2}} + \frac{H_{pv}}{(n_{pv} + 1)} [(\mathbf{e}^{\text{tr}} : \mathbf{e}^{\text{pl}}) \delta_{pv}]^{n_{pv}+1}. \quad (5)$$

In (5), parameters  $H_v$  and  $n_v$  describe the interactions between martensite variants,  $H_p$  and  $n_p$  describe the interactions between slip systems,  $H_{pv}$  and  $n_{pv}$  describe the interactions between martensite variants and slip systems as well as the interactions between and inside grains, and  $\delta_{pv} = \text{sgn}(\mathbf{e}^{\text{tr}} : \mathbf{e}^{\text{pl}})$ . The rates of macroscopic transformation strain  $\dot{\mathbf{e}}^{\text{tr}}$  and macroscopic plastic strain  $\dot{\mathbf{e}}^{\text{pl}}$  are expressed as follows

$$\dot{\mathbf{e}}^{\text{tr}} = \dot{\xi} \bar{\mathbf{e}}_{\text{tr}} = \dot{\xi} \varepsilon_L \mathbf{N}^{\text{tr}}, \quad (6)$$

$$\dot{\mathbf{e}}^{\text{pl}} = (1 - \xi) \dot{\mathbf{e}}_{\text{pl}} = (1 - \xi) \dot{p} \mathbf{N}^{\text{pl}}, \quad (7)$$

where  $\varepsilon_L$  is the maximum uniaxial transformation strain,  $\dot{p}$  is the rate of the magnitude of plastic strain,  $\mathbf{N}^{\text{tr}}$  and  $\mathbf{N}^{\text{pl}}$  are tensors which non Mises norms are one and that gives, respectively, the direction of transformation and plasticity. It is worth mentioning that (6) and (7) are based on the assumptions that the rate of transformation strain is proportional only to that of the volume fraction of martensite; and the rate of plastic strain is proportional only to that of the magnitude of cumulative plastic strain.

## 2.2. Internal constraints and Lagrangian

The state variables are subjected to the following physical constraints:

**Constraint 1 :** the volume fraction of any single phase cannot be less than 0 or more than 1, which is expressed by the inequalities

$$\xi \geq 0 \text{ and } (1 - \xi) \geq 0. \quad (8)$$

**Constraint 2 :** the two phases are assumed to be arranged in series. The total strain tensor is therefore obtained from the local strain in each phase using Voigt rule of mixture,

$$\mathbf{e} = (1 - \xi) \mathbf{e}_a + \xi \mathbf{e}_m. \quad (9)$$

The above linear constraints derive from the following constraints potential:

$$\Phi_{\text{KT}} = -\lambda_1 \xi - \lambda_2 (1 - \xi) - \lambda : [(1 - \xi) \mathbf{e}_a + \xi \mathbf{e}_m - \mathbf{e}], \quad (10)$$

where  $\lambda_1$ ,  $\lambda_2$ , and  $\lambda$  are Lagrange multipliers obeying the Kuhn-Tucker conditions

$$\lambda_1 \geq 0, \lambda_1 \xi = 0, \lambda_2 \geq 0, \lambda_2 (1 - \xi) = 0, \text{ and}$$

$$\lambda : [(1 - \xi) \mathbf{e}_a + \xi \mathbf{e}_m - \mathbf{e}] = 0. \quad (11)$$

The following Lagrangian is then constructed as the sum of the Helmholtz free energy, interaction energy and constraints

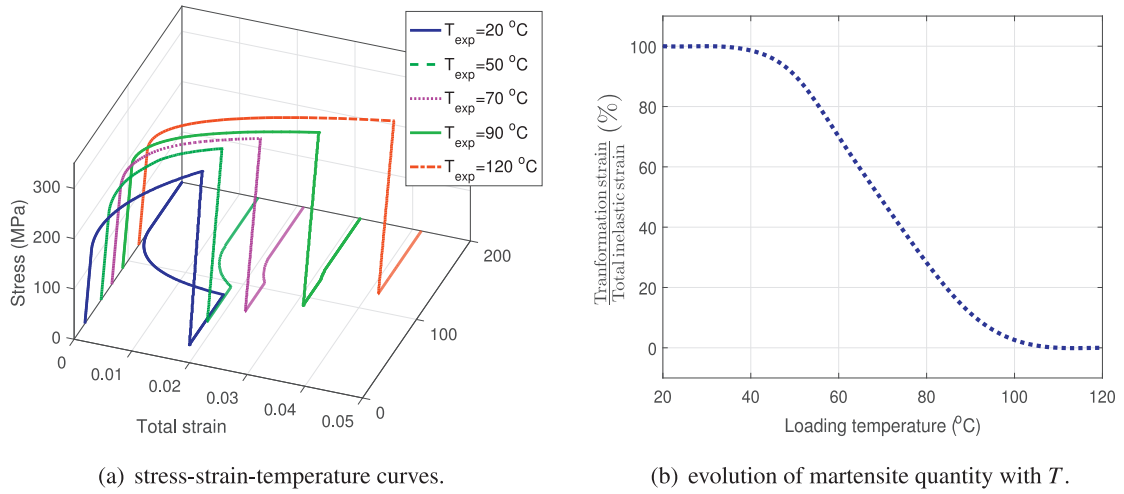


Fig. 2. Competition between transformation and plasticity.

potential:

$$\begin{aligned}
 \mathcal{L} &= \Phi + \Phi_{KT} \\
 &= \frac{(1-\xi)}{2} [(\boldsymbol{\varepsilon}_a - \bar{\boldsymbol{\varepsilon}}_{pl}) : \mathbf{K}_a : (\boldsymbol{\varepsilon}_a - \bar{\boldsymbol{\varepsilon}}_{pl})] \\
 &\quad + \frac{\xi}{2} [(\boldsymbol{\varepsilon}_m - \bar{\boldsymbol{\varepsilon}}_{tr}) : \mathbf{K}_m : (\boldsymbol{\varepsilon}_m - \bar{\boldsymbol{\varepsilon}}_{tr})] + \xi \zeta (T - T_0) \\
 &\quad + \frac{H_v}{(n_v + 1)} (\boldsymbol{\varepsilon}^{tr} : \boldsymbol{\varepsilon}^{tr})^{\frac{n_v+1}{2}} + \frac{H_p}{(n_p + 1)} (\boldsymbol{\varepsilon}^{pl} : \boldsymbol{\varepsilon}^{pl})^{\frac{n_p+1}{2}} \\
 &\quad + \frac{H_{pv}}{(n_{pv} + 1)} [(\boldsymbol{\varepsilon}^{tr} : \boldsymbol{\varepsilon}^{pl}) \delta_{pv}]^{n_{pv}+1} \\
 &\quad - \lambda_1 \xi - \lambda_2 (1 - \xi) - \lambda : [(1 - \xi) \boldsymbol{\varepsilon}_a + \xi \boldsymbol{\varepsilon}_m - \boldsymbol{\varepsilon}]. \quad (12)
 \end{aligned}$$

### 2.3. State equations

From considerations of thermodynamic consistency, the state equations are derived as follows:

$$\frac{\partial \mathcal{L}}{\partial \boldsymbol{\varepsilon}} = \boldsymbol{\sigma} \Rightarrow \boldsymbol{\lambda} = \boldsymbol{\sigma}, \quad (13)$$

$$-\frac{\partial \mathcal{L}}{\partial \boldsymbol{\varepsilon}_a} = \mathbf{0} \Rightarrow (1 - \xi) [\mathbf{K}_a : (\boldsymbol{\varepsilon}_a - \bar{\boldsymbol{\varepsilon}}_{pl}) - \boldsymbol{\lambda}] = \mathbf{0}, \quad (14)$$

$$-\frac{\partial \mathcal{L}}{\partial \boldsymbol{\varepsilon}_m} = \mathbf{0} \Rightarrow \xi [\mathbf{K}_m : (\boldsymbol{\varepsilon}_m - \bar{\boldsymbol{\varepsilon}}_{tr}) - \boldsymbol{\lambda}] = \mathbf{0}, \quad (15)$$

$$-\frac{\partial \mathcal{L}}{\partial \boldsymbol{\lambda}} = \mathbf{0} \Rightarrow (1 - \xi) \boldsymbol{\varepsilon}_a + \xi \boldsymbol{\varepsilon}_m - \boldsymbol{\varepsilon} = \mathbf{0}, \quad (16)$$

$$-\frac{\partial \mathcal{L}}{\partial \xi} = \mathcal{A}_{tr}, \quad (17)$$

$$-\frac{\partial \mathcal{L}}{\partial p} = \mathcal{A}_{pl}, \quad (18)$$

$$-\frac{\partial \mathcal{L}}{\partial \bar{\boldsymbol{\varepsilon}}_{tr}} = \boldsymbol{\eta}^{tr}, \quad (19)$$

$$-\frac{\partial \mathcal{L}}{\partial \bar{\boldsymbol{\varepsilon}}_{pl}} = \boldsymbol{\eta}^{pl}. \quad (20)$$

The martensitic transformation and plastic deformation being the only dissipative processes, the corresponding thermodynamic forces  $\mathcal{A}_{tr}$  and  $\mathcal{A}_{pl}$  are not zero in general. Using Eqs. (13)–(16), these thermodynamics forces and the stress-strain relation are

expressed as follows:

$$\begin{aligned}
 \mathcal{A}_{tr} &= \frac{G_{ma}}{6} \sigma_{eq}^2 + \frac{\kappa_{ma}}{2} \sigma_h^2 + \boldsymbol{\sigma} : (\bar{\boldsymbol{\varepsilon}}_{tr} - \bar{\boldsymbol{\varepsilon}}_{pl}) - \zeta (T - T_0) \\
 &\quad - H_v (\bar{\boldsymbol{\varepsilon}}_{tr} : \boldsymbol{\varepsilon}^{tr}) (\boldsymbol{\varepsilon}^{tr} : \boldsymbol{\varepsilon}^{tr})^{\frac{n_v-1}{2}} \\
 &\quad - H_{pv} \delta_{pv} (\bar{\boldsymbol{\varepsilon}}_{tr} : \boldsymbol{\varepsilon}^{pl}) [(\boldsymbol{\varepsilon}^{tr} : \boldsymbol{\varepsilon}^{pl}) \delta_{pv}]^{n_{pv}} + (\lambda_1 - \lambda_2), \quad (21)
 \end{aligned}$$

$$\begin{aligned}
 \mathcal{A}_{pl} &= (1 - \xi) \left[ \boldsymbol{\sigma} - H_p (\boldsymbol{\varepsilon}^{pl} : \boldsymbol{\varepsilon}^{pl})^{\frac{n_p-1}{2}} \boldsymbol{\varepsilon}^{pl} - H_{pv} \delta_{pv} [(\boldsymbol{\varepsilon}^{tr} : \boldsymbol{\varepsilon}^{pl}) \delta_{pv}]^{n_{pv}} \boldsymbol{\varepsilon}^{tr} \right] \\
 &\quad : \mathbf{N}^{pl}, \quad (22)
 \end{aligned}$$

$$\boldsymbol{\sigma} = \mathbf{K}_{eq} : [\boldsymbol{\varepsilon} - \boldsymbol{\varepsilon}^{tr} - \boldsymbol{\varepsilon}^{pl}], \quad (23)$$

$$\mathbf{K}_{eq} = [(1 - \xi) \mathbf{K}_a^{-1} + \xi \mathbf{K}_m^{-1}]^{-1}, \quad (24)$$

where  $G_{ma} = \frac{1}{G_m} - \frac{1}{G_a}$  and  $\kappa_{ma} = \frac{1}{\kappa_m} - \frac{1}{\kappa_a}$  are the differences in inverse shear and inverse bulk moduli of the two phases. The von Mises effective stress  $\sigma_{eq}$  and hydrostatic stress  $\sigma_h$  are given by

$$\sigma_{eq} = \sqrt{\frac{3}{2} (\boldsymbol{\sigma}^{dev} : \boldsymbol{\sigma}^{dev})}, \quad (25)$$

$$\sigma_h = \frac{1}{3} \text{tr}(\boldsymbol{\sigma}), \quad (26)$$

where  $\boldsymbol{\sigma}^{dev} = \boldsymbol{\sigma} - \sigma_h \mathbf{I}$  is the deviatoric stress.

### 2.4. Pseudopotential of dissipation and loading conditions

Within the framework of generalized standard materials, the thermodynamic forces  $\mathcal{A}_{tr}$  and  $\mathcal{A}_{pl}$  are taken as sub-gradients of a real-valued convex pseudo-potential of dissipation  $\mathcal{D}$  with respect to the rate variables  $\dot{\xi}$  and  $\dot{p}$ .

**Definition 1.** a real-valued convex function  $f : \mathcal{C} \rightarrow \mathbb{R}$  is said to have a sub-gradient  $\mathcal{U}$  at point  $\mathbf{x}_0$  in a set  $\mathcal{C}$  of  $\mathbb{R}^n$  if  $\mathcal{U} \in \mathbb{R}^n$  verifies the inequality  $f(\mathbf{x}) \geq f(\mathbf{x}_0) + \langle \mathcal{U}, \mathbf{x} - \mathbf{x}_0 \rangle$  for all  $\mathbf{x} \in \mathcal{C}$ , where  $\langle \cdot, \cdot \rangle$  denotes the dot product in  $\mathbb{R}^n$ .

The pseudo-potential  $\mathcal{D}$  is required to verify the following mathematical properties:

**Property 1.**  $\mathcal{D} = \mathcal{D}(u_1, u_2, \dots, u_n)$  must be convex and lower semi-continuous with respect to its variables.

This means that  $\mathcal{D} : \mathcal{C} \rightarrow \mathbb{R} \cup \{-\infty, +\infty\}$  must be an extended-real-valued and convex function for which  $f(\mathbf{x}) \leq \lim_{i \rightarrow +\infty} f(\mathbf{x}_i)$  at



**Table 2**  
Material parameters.

Parameter	Value	Parameter	Value
$E_m$	260 GPa	$E_a$	130 GPa
$\sigma_m^{\text{tr}}$	130 MPa	$\sigma_a^{\text{tr}}$	72 MPa
$\zeta_m$	0.086 MPa/°C	$\zeta_a$	0.043 MPa/°C
$\beta$	0.45 MPa/°C	$\sigma_a^{\text{pl}}$	250 MPa
$M_s^0$	0 °C	$A_s^0$	95 °C
$H_v$	1165.7 MPa	$n_v$	0.52
$H_p$	497.8 MPa	$n_p$	0.45
$H_{pv}$	19567 MPa	$n_{pv}$	0.48
$H_s$	5000 MPa	$H_x$	13.12 MPa
$\nu$	0.3		

any point  $\mathbf{x} \in \mathcal{C}$ , for every sequence  $\mathbf{x}_1, \mathbf{x}_2, \mathbf{x}_3, \dots$  in  $\mathcal{C}$  such that  $\mathbf{x}_i$  converges to  $\mathbf{x}$  and the limits of  $f(\mathbf{x}_1), f(\mathbf{x}_2), f(\mathbf{x}_3), \dots$  exist in  $[-\infty, +\infty]$ . The lower semi-continuity property is guaranteed if  $\mathcal{D}$  is continuous.

**Property 2.**  $\mathcal{D}$  must be positive and equal to zero at the origin.

This means that  $\mathcal{D}(\mathbf{x}) \geq 0$ ,  $\forall \mathbf{x} = (x_1, x_2, \dots, x_n) \in \mathcal{C}$ ; and  $\mathcal{D}(\mathbf{x}) = 0$ , for  $\mathbf{x} = 0$ .

**Property 3.**  $\mathcal{D}$  must be positively homogeneous of degree one for rate-independent processes.

This means that  $\mathcal{D}(\mu(x_1, x_2, \dots, x_n)) = \mu \mathcal{D}(x_1, x_2, \dots, x_n)$ ,  $\forall \mu > 0$ .

The first two requirements on  $\mathcal{D}$  ensure that the evolution equations derived within the framework of generalized standard materials satisfy the second principle of thermodynamics. In this work,  $\mathcal{D}$  is defined as follows:

$$\mathcal{D}(\dot{\xi}, \dot{p}) = D_a^{\text{tr}} |\dot{\xi}| + D_a^{\text{pl}} |\dot{p}|, \quad (27)$$

where the functions  $D_a^{\text{tr}}$ ,  $\alpha = \{a, m\}$ , and  $D_a^{\text{pl}}$  are given by

$$D_m^{\text{tr}}(p) = \sigma_m^{\text{tr}} \varepsilon_L + \zeta_m (T_0 - M_s^0) + H_s p^2, \text{ for } \dot{\xi} > 0, \quad (28)$$

$$D_a^{\text{tr}}(\xi) = \sigma_a^{\text{tr}} \varepsilon_L - \zeta_a (T_0 - A_s^0) - H_x \xi, \text{ for } \dot{\xi} < 0, \quad (29)$$

$$D_a^{\text{pl}}(T) = \sigma_a^{\text{pl}} - \beta T > 0. \quad (30)$$

To capture more accurately the reverse transformation and avoid physical inconsistencies, the present work considers two different critical stresses  $\sigma_m^{\text{tr}}$  and  $\sigma_a^{\text{tr}}$  for forward and reverse phase transformations, respectively. It is well known from experiments like Khalil et al. (2013) that plastic slip has detrimental effect on phase transformation. In order to take into account this phenomenon that has been ignored in existing Fe-SMA models, the present work introduces the new term “ $H_s p^2$ ” in (28). The incorporation of the term “ $H_x \xi$ ” in (29) is motivated by the experimental results of Nishimura et al. (1999) highlighting a shift of the  $A_s$  line towards the lower temperature side with the increase of the martensite quantity;  $\zeta_a$  being unaffected. In (30),  $\sigma_a^{\text{pl}}$  is the plastic yield strength of austenite, and  $\beta$  is a parameter controlling the linear decrease with temperature of the plastic yield strength, with  $< x > = x$  if  $x$  is positive and 0 otherwise. From the relations

$$\begin{aligned} \mathcal{A}_{\text{tr}} &= -\frac{\partial \mathcal{L}}{\partial \xi} \text{ and } \mathcal{A}_{\text{tr}} \in \partial_{\xi} \mathcal{D}, \\ \mathcal{A}_{\text{pl}} &= -\frac{\partial \mathcal{L}}{\partial p} \text{ and } \mathcal{A}_{\text{pl}} \in \partial_p \mathcal{D}, \end{aligned} \quad (31)$$

the following loading functions are obtained:

$$\mathcal{F}_m^{\text{tr}} = \mathcal{A}_{\text{tr}} - D_m^{\text{tr}}, \text{ for forward phase transformation,} \quad (32)$$

$$\mathcal{F}_a^{\text{tr}} = -\mathcal{A}_{\text{tr}} - D_a^{\text{tr}}, \text{ for reverse phase transformation,} \quad (33)$$

$$\mathcal{F}_a^{\text{pl}} = \mathcal{A}_{\text{pl}} - D_a^{\text{pl}}, \text{ for plastic deformation.} \quad (34)$$

Considering the constraints (8) and (9), the model is completed by the following Kuhn–Tucker conditions associated to the dissipative variables:

- $\mathcal{F}_m^{\text{tr}} \leq 0$ ,  $\dot{\xi} \geq 0$  and  $\dot{\xi} \mathcal{F}_m^{\text{tr}} = 0$  for forward transformation,
- $\mathcal{F}_a^{\text{tr}} \leq 0$ ,  $-\dot{\xi} \geq 0$  and  $(-\dot{\xi}) \mathcal{F}_a^{\text{tr}} = 0$  for reverse transformation,
- $\mathcal{F}_a^{\text{pl}} \leq 0$ ,  $\dot{p} \geq 0$  and  $\dot{p} \mathcal{F}_a^{\text{pl}} = 0$  for plastic deformation.

The transformation and plastic directions are obtained by using the *generalized normality rule*. To this end, we consider the two vectors

$$\boldsymbol{\eta}^{\text{tr}} = \xi \left[ \boldsymbol{\sigma} - H_v (\boldsymbol{\varepsilon}^{\text{tr}} : \boldsymbol{\varepsilon}^{\text{tr}})^{\frac{n_v-1}{2}} \boldsymbol{\varepsilon}^{\text{tr}} - H_{pv} \delta_{pv} [(\boldsymbol{\varepsilon}^{\text{tr}} : \boldsymbol{\varepsilon}^{\text{pl}}) \delta_{pv}]^{n_{pv}} \boldsymbol{\varepsilon}^{\text{pl}} \right], \quad (35)$$

$$\boldsymbol{\eta}^{\text{pl}} = (1 - \xi) \left[ \boldsymbol{\sigma} - H_p (\boldsymbol{\varepsilon}^{\text{pl}} : \boldsymbol{\varepsilon}^{\text{pl}})^{\frac{n_p-1}{2}} \boldsymbol{\varepsilon}^{\text{pl}} - H_{pv} \delta_{pv} [(\boldsymbol{\varepsilon}^{\text{tr}} : \boldsymbol{\varepsilon}^{\text{pl}}) \delta_{pv}]^{n_{pv}} \boldsymbol{\varepsilon}^{\text{tr}} \right]. \quad (36)$$

**Remark 1.** for martensite transformation, we are interested in defining the flow direction only for the case  $\xi > 0$ .

**Remark 2.** for plastic deformation, the case  $\xi = 1$  is not at stake here, since it corresponds to complete martensitic transformation, while plasticity is considered only for austenite.

Using these two remarks, we define  $\mathbf{V}^{\text{tr}} = \frac{1}{\xi} \boldsymbol{\eta}^{\text{tr}}$  and  $\mathbf{V}^{\text{pl}} = \frac{1}{(1-\xi)} \boldsymbol{\eta}^{\text{pl}}$ , from which  $\mathbf{N}^{\text{tr}}$  and  $\mathbf{N}^{\text{pl}}$  are constructed as follows

$$\mathbf{N}^{\text{tr}} = \begin{cases} \frac{3}{2} \frac{\mathbf{V}_{\text{tr}}^{\text{dev}}}{V_{\text{tr}}^{\text{eq}}}, & \text{if } \dot{\xi} > 0, \\ \frac{\boldsymbol{\varepsilon}^{\text{tr}}}{\xi}, & \text{if } \dot{\xi} < 0, \end{cases} \quad (37)$$

and

$$\mathbf{N}^{\text{pl}} = \begin{cases} \frac{3}{2} \frac{\mathbf{V}_{\text{pl}}^{\text{dev}}}{V_{\text{pl}}^{\text{eq}}}, & \text{if } \sigma_{\text{eq}} \neq 0, \\ \frac{\boldsymbol{\varepsilon}^{\text{pl}}}{\varepsilon_{\text{pl}}^{\text{eq}}}, & \text{otherwise.} \end{cases} \quad (38)$$

In the above two equations,  $\mathbf{V}_{\alpha}^{\text{dev}}$  and  $V_{\alpha}^{\text{eq}}$  are, respectively, the deviatoric part and von Mises norm of the first order tensor  $\mathbf{V}^{\alpha}$ , with  $\alpha = \{\text{tr}, \text{pl}\}$ .

**Remark 3.** defining the tensors  $\mathbf{V}^{\text{tr}} = \frac{1}{\xi + \nu} \boldsymbol{\eta}^{\text{tr}}$  and  $\mathbf{V}^{\text{pl}} = \frac{1}{(1-\xi) + \nu} \boldsymbol{\eta}^{\text{pl}}$ , with  $\nu \rightarrow 0$ , would also remove the singularities.

The constitutive model is summarized in Table 1.

### 3. Time-integration of the model

The proposed model needs to be integrated in commercial software for the design of Fe-SMA structures. A common way is to implement, in a discrete form, the constitutive equations in a user defined material subroutine (UMAT) that is appended to “finite element”-based software ABAQUS. The time-discrete integration of the constitutive equations was accomplished using an implicit numerical algorithm (Zaki, 2012; Gu et al., 2015).

#### 3.1. Algorithmic setup

It is well known in computational mechanics that stability is guaranteed with backward Euler method (BEM). The BEM have several subcategories among which the “Return Mapping Algorithms” (RMA) have the advantage to be implicit not only in time steps but also in iterations. Therefore, the convexity of the loading functions are sufficient conditions to ensure convergence of RMAs. However, due to the strong nonlinearity of the model and the coupling between plasticity and phase transformation, the RMA

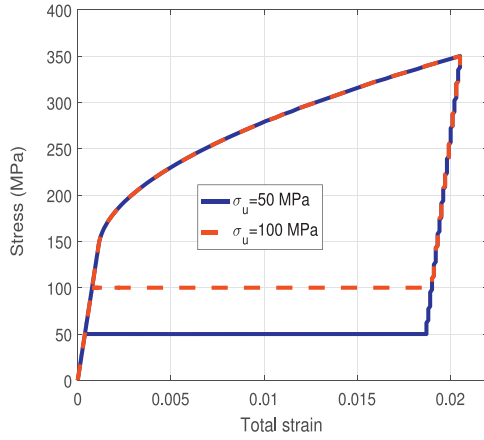
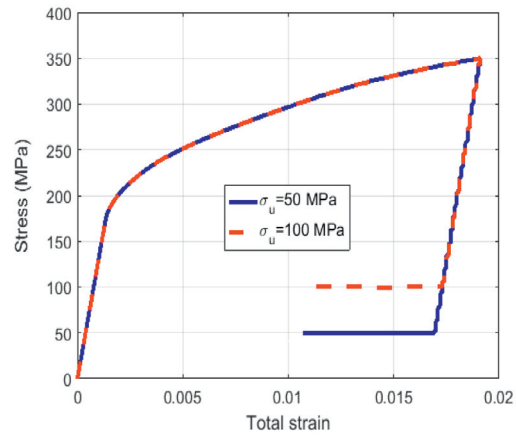
(a) partial unloadings for  $T=20\text{ }^{\circ}\text{C}$ .(b) partial unloadings for  $T=50\text{ }^{\circ}\text{C}$ .

Fig. 3. Recovery of inelastic transformation strain at non zero stress.

is implemented in its “convex cutting plane” type rather than its cumbersome “closest point projection” approach. The detection of active loading surfaces and the implementation of appropriate consistency conditions are inspired from computational multi-surface plasticity (Simo et al., 1988). To this end, a time-discrete incremental solution procedure is used whereby the load is divided into  $N$  increments with a known initial state. Starting with load increment at  $n = 0$ , the values of the state variables are calculated iteratively for  $n = 1 \dots N$  using an elastic predictor-inelastic corrector scheme. If  $\Delta$  denotes finite incrementation, the uniaxial time-discrete equations of the model can be written as follows:

#### 1. Initialization:

Set  $\mathbf{e}_{n+1} = \mathbf{e}_n + \Delta \mathbf{e}$ , and  $T_{n+1} = T_n + \Delta T$ ,

Set  $\xi_{n+1}^{(0)} = \xi_n$ ,  $\mathbf{e}_{n+1}^{\text{tr}(0)} = \mathbf{e}_n^{\text{tr}}$ ,  $p_{n+1}^{(0)} = p_n$ ,  $\mathbf{e}_{n+1}^{\text{pl}(0)} = \mathbf{e}_n^{\text{pl}}$ , and  $\mathbf{K}_{\text{eq},n+1}^{(0)} =$

$\mathbf{K}_{\text{eq},n}$ .

#### 2. Elastic prediction:

Calculate  $\boldsymbol{\sigma}_{n+1}^{(0)} = \mathbf{K}_{\text{eq},n+1}^{(0)} : [\mathbf{e}_{n+1} - \mathbf{e}_{n+1}^{\text{tr}(0)} - \mathbf{e}_{n+1}^{\text{pl}(0)}]$ ,

Set  $k = 0$

Calculate  $\mathcal{F}_{m,n+1}^{(k)}$ ,  $\mathcal{F}_{a,n+1}^{(k)}$ , and  $\mathcal{F}_{p,n+1}^{(k)}$  using the trial state variables.

#### 3. Consistency conditions:

##### (a) Active loading set

IF  $\mathcal{F}_{m,n+1}^{(k)} < 0$ , and  $\mathcal{F}_{a,n+1}^{(k)} < 0$  and  $\mathcal{F}_{p,n+1}^{(k)} < 0$ , THEN elastic response,

IF  $\xi_{n+1}^{(k)} < 1$  and  $\mathcal{F}_{m,n+1}^{(k)} > 0$ , THEN direct phase transformation is assumed to be active,

IF  $\xi_{n+1}^{(k)} > 0$  and  $\mathcal{F}_{a,n+1}^{(k)} > 0$ , THEN reverse phase transformation is assumed to be active,

IF  $\mathcal{F}_{p,n+1}^{(k)} > 0$ , THEN plastic deformation is assumed to be active.

##### (b) Increments of internal state variables

IF transformation without plastic deformation, THEN  $\Delta \xi_{n+1}^{(k)}$  is given by the consistency condition  $\mathcal{F}_{a,n+1}^{(k+1)} = 0$  with  $\Delta p_{n+1}^{(k)} = 0$ , and  $\alpha = \{a, m\}$

IF plastic deformation without transformation, THEN  $\Delta p_{n+1}^{(k)}$  is given by the consistency condition  $\mathcal{F}_{p,n+1}^{(k+1)} = 0$  with  $\Delta \xi_{n+1}^{(k)} = 0$ ,

IF transformation and plasticity, THEN  $\Delta \xi_{n+1}^{(k)}$  and  $\Delta p_{n+1}^{(k)}$  are given by the consistency conditions  $\{\mathcal{F}_{a,n+1}^{(k+1)} = 0, \mathcal{F}_{p,n+1}^{(k+1)} = 0\}$ , with  $\alpha = \{a, m\}$

Set  $\mathbf{e}_{n+1}^{\text{tr}(k+1)} = \mathbf{e}_{n+1}^{\text{tr}(k)} + \Delta \xi_{n+1}^{(k)} \varepsilon_L \mathbf{N}^{\text{tr}(k)}$ ,

Set  $\mathbf{e}_{n+1}^{\text{pl}(k+1)} = \mathbf{e}_{n+1}^{\text{pl}(k)} + (1 - \xi) \Delta p_{n+1}^{(k)} \mathbf{N}_{n+1}^{\text{pl}(k)}$ .

##### (c) Positivity of the multipliers

IF direct transformation and  $\Delta \xi_{n+1}^{(k)} < 0$ , THEN reset  $\Delta \xi_{n+1}^{(k)}$  to zero, direct transformation is inactive,

IF reverse transformation and  $\Delta \xi_{n+1}^{(k)} > 0$ , THEN reset  $\Delta \xi_{n+1}^{(k)}$  to zero, reverse transformation is inactive,

IF plastic deformation and  $\Delta p_{n+1}^{(k)} < 0$ , THEN reset  $\Delta p_{n+1}^{(k)}$  to zero, plasticity is inactive.

IF  $\Delta \xi_{n+1}^{(k)}$  or  $\Delta p_{n+1}^{(k)}$  is reset to zero, THEN go to (a) ELSE continue.

##### (d) Consistency with the constraints on the state variables

IF direct transformation and  $\xi_n + \Delta \xi_{n+1}^{(k)} > 1$ , THEN set  $\Delta \xi_{n+1}^{(k)} = 1 - \xi_n$ .

IF reverse transformation and  $\xi_n + \Delta \xi_{n+1}^{(k)} < 0$ , THEN set  $\Delta \xi_{n+1}^{(k)} = -\xi_n$ .

##### (e) Stress update

Calculate  $\mathbf{K}_{\text{eq},n+1}^{(k+1)} = \left[ (1 - \xi_{n+1}^{(k+1)}) \mathbf{K}_a^{-1} + \xi_{n+1}^{(k+1)} \mathbf{K}_m^{-1} \right]^{-1}$ ,

Calculate  $\boldsymbol{\sigma}_{n+1}^{(k+1)} = \mathbf{K}_{\text{eq},n+1}^{(k+1)} : [\mathbf{e}_{n+1} - \mathbf{e}_{n+1}^{\text{tr}(k+1)} - \mathbf{e}_{n+1}^{\text{pl}(k+1)}]$ .

##### (f) Set $k = k + 1$ .

##### (g) Repeat steps (a)–(f) until consistency with the loading conditions and intrinsic constraints on $\xi$ are achieved.

### 3.2. Consistency conditions

The consistency conditions allow to compute the increment of internal variables, thus to update the stress. From the stress-strain relations

$$\begin{cases} \boldsymbol{\sigma} = \mathbf{K}_{\text{eq}} \mathbf{e}^{\text{el}}, \\ \mathbf{K}_{\text{eq}} = [(1 - \xi) \mathbf{K}_a^{-1} + \xi \mathbf{K}_m^{-1}]^{-1}, \end{cases} \Rightarrow \begin{cases} \mathbf{e}^{\text{el}} = \mathbf{S}_{\text{eq}} \boldsymbol{\sigma}, \\ \mathbf{S}_{\text{eq}} = (1 - \xi) \mathbf{K}_a^{-1} + \xi \mathbf{K}_m^{-1}, \end{cases} \quad (39)$$

the following expressions of the stress increment is established:

$$\Delta \boldsymbol{\sigma} = \mathbf{K}_{\text{eq}} : [\Delta \boldsymbol{\varepsilon} - (\mathbf{S}_{\text{ma}} : \boldsymbol{\sigma} + \varepsilon_L \mathbf{N}^{\text{tr}}) \Delta \xi - (1 - \xi) \mathbf{N}^{\text{pl}} \Delta p], \quad (40)$$

where  $\mathbf{S}_{\text{ma}} = \mathbf{K}_m^{-1} - \mathbf{K}_a^{-1}$ . In the following sections we will denote:

$$\begin{cases} \mathbf{R}_{\xi} = \mathbf{S}_{\text{ma}} : \boldsymbol{\sigma} + \varepsilon_L \mathbf{N}^{\text{tr}}, \\ \mathbf{R}_p = (1 - \xi) \mathbf{N}^{\text{pl}}, \\ \mathcal{F}_{\alpha,Y}^{\text{tr}} = \frac{\partial \mathcal{F}_{\alpha}^{\text{tr}}}{\partial Y}, \text{ with } Y = \{\xi, p, T, \boldsymbol{\sigma}\}, \\ \mathcal{F}_{\alpha,Y}^{\text{pl}} = \frac{\partial \mathcal{F}_{\alpha}^{\text{pl}}}{\partial Y}, \text{ with } Y = \{\xi, p, T, \boldsymbol{\sigma}\}. \end{cases} \quad (41)$$

As its name suggests, the objective of the RMA is to find the increments of state variables that will bring back the loading point

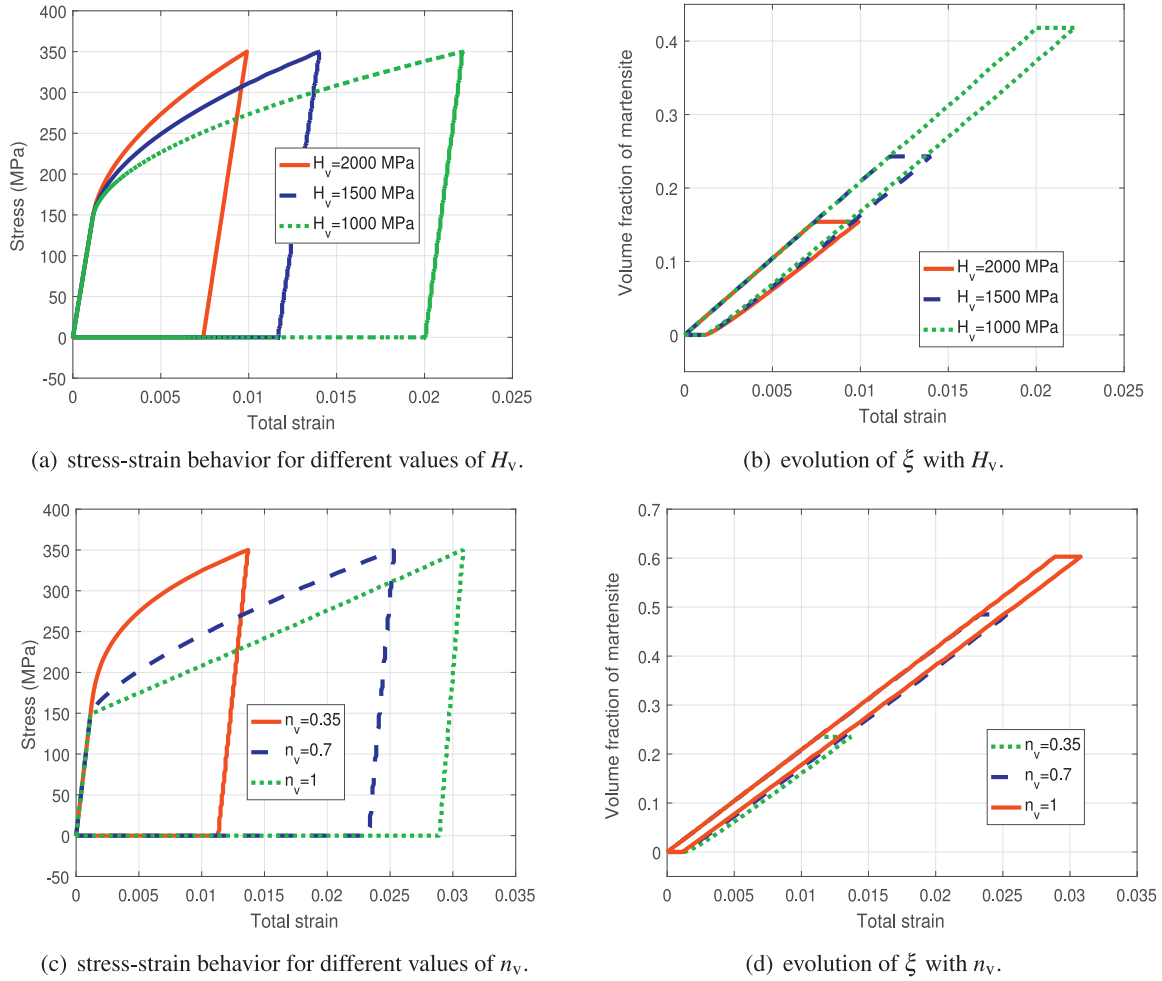


Fig. 4. Influence of  $H_v$  and  $n_v$  on Fe-SMA behavior at  $T = 20$  °C.

at which the transformation and/or plastic loading function is positive on the loading surface. Starting from  $\mathcal{F}_{n+1}^{(0)} > 0$  at the elastic prediction, new increments of stress and internal variables are calculated iteratively and implicitly until convergence is reached, using

$$\begin{aligned} \mathcal{F}_{n+1}^{(k+1)} = \mathcal{F}_{n+1}^{(k)} + \frac{\partial \mathcal{F}}{\partial \boldsymbol{\sigma}} \bigg|_{n+1}^{(k)} : \Delta \boldsymbol{\sigma}_{n+1}^{(k)} + \frac{\partial \mathcal{F}}{\partial \xi} \bigg|_{n+1}^{(k)} \Delta \xi_{n+1}^{(k)} \\ + \frac{\partial \mathcal{F}}{\partial p} \bigg|_{n+1}^{(k)} \Delta p_{n+1}^{(k)} + \frac{\partial \mathcal{F}}{\partial T} \bigg|_{n+1}^{(k)} \Delta T_{n+1}^{(k)} \simeq 0. \end{aligned} \quad (42)$$

The increments of temperature and total strain being fixed by the solver during the whole inelastic correction, their variations are null, i.e.  $\Delta T_{n+1}^{(k)} = 0$  and  $\Delta \boldsymbol{\epsilon}_{n+1}^{(k)} = 0$ . Hence, applying the multivariable chain rule to  $\mathcal{F}_{\alpha n+1}^{tr(k)}$  and  $\mathcal{F}_{a n+1}^{pl(k)}$ , using (40) and (41), and gathering the factorial terms of  $\Delta \xi_{n+1}^{(k)}$  and  $\Delta p_{n+1}^{(k)}$ , the following system is established:

$$\begin{cases} \mathcal{F}_{\alpha n+1}^{tr(k)} + \Lambda_{\xi n+1}^{(k)} \Delta \xi_{n+1}^{(k)} + \Lambda_{p n+1}^{(k)} \Delta p_{n+1}^{(k)} \simeq 0, \\ \mathcal{F}_{a n+1}^{pl(k)} + \Omega_{\xi n+1}^{(k)} \Delta \xi_{n+1}^{(k)} + \Omega_{p n+1}^{(k)} \Delta p_{n+1}^{(k)} \simeq 0, \end{cases} \quad (43)$$

where,

$$\Lambda_{\xi} = \frac{\partial \mathcal{F}_{\alpha}^{tr}}{\partial \xi} - \frac{\partial \mathcal{F}_{\alpha}^{tr}}{\partial \boldsymbol{\sigma}} : (\mathbf{K}_{eq} \mathbf{R}_{\xi}), \quad (44)$$

$$\Lambda_p = \frac{\partial \mathcal{F}_{\alpha}^{tr}}{\partial p} - \frac{\partial \mathcal{F}_{\alpha}^{tr}}{\partial \boldsymbol{\sigma}} : (\mathbf{K}_{eq} \mathbf{R}_p), \quad (45)$$

$$\Omega_{\xi} = \frac{\partial \mathcal{F}_{a}^{pl}}{\partial \xi} - \frac{\partial \mathcal{F}_{a}^{pl}}{\partial \boldsymbol{\sigma}} : (\mathbf{K}_{eq} \mathbf{R}_{\xi}), \quad (46)$$

$$\Omega_p = \frac{\partial \mathcal{F}_{a}^{pl}}{\partial p} - \frac{\partial \mathcal{F}_{a}^{pl}}{\partial \boldsymbol{\sigma}} : (\mathbf{K}_{eq} \mathbf{R}_p). \quad (47)$$

The values of  $\Delta \xi_{n+1}^{(k)}$  and  $\Delta p_{n+1}^{(k)}$  are obtained by solving (43) as follows:

- IF both phase transformation and plasticity are activated, THEN solving the system (43) gives

$$\begin{cases} \Delta \xi_{n+1}^{(k)} = \frac{\Lambda_{p n+1}^{(k)}}{\chi_{n+1}^{(k)}} \mathcal{F}_{a n+1}^{pl(k)} - \frac{\Omega_{p n+1}^{(k)}}{\chi_{n+1}^{(k)}} \mathcal{F}_{\alpha n+1}^{tr(k)}, \\ \Delta p_{n+1}^{(k)} = \frac{\Omega_{\xi n+1}^{(k)}}{\chi_{n+1}^{(k)}} \mathcal{F}_{\alpha n+1}^{tr(k)} - \frac{\Lambda_{\xi n+1}^{(k)}}{\chi_{n+1}^{(k)}} \mathcal{F}_{a n+1}^{pl(k)}, \end{cases} \quad (48)$$

- IF only phase transformation is activated, THEN solving the first equation of (43) gives

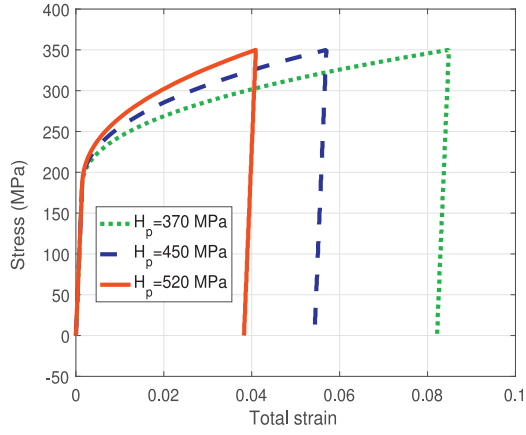
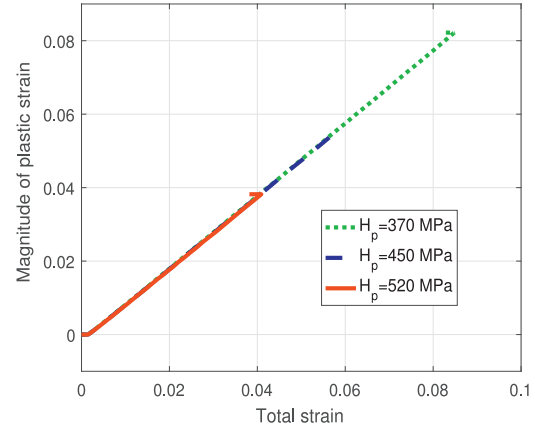
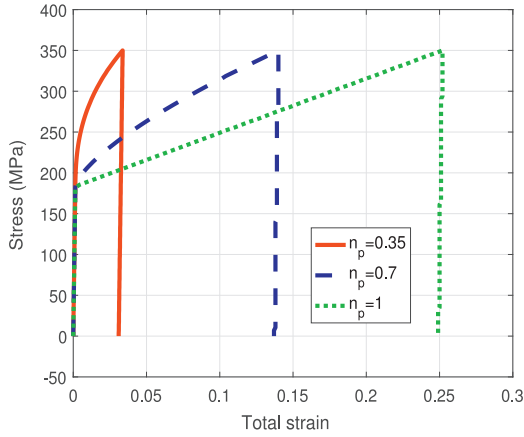
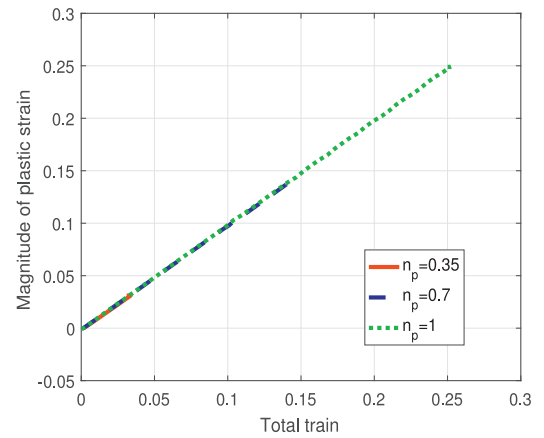
$$\begin{cases} \Delta \xi_{n+1}^{(k)} = -\frac{1}{\Lambda_{\xi n+1}^{(k)}} \mathcal{F}_{\alpha n+1}^{tr(k)}, \\ \Delta p_{n+1}^{(k)} = 0, \end{cases} \quad (49)$$

- IF only plasticity are activated, THEN solving the second equation of (43) yields

$$\begin{cases} \Delta p_{n+1}^{(k)} = -\frac{1}{\Omega_{p n+1}^{(k)}} \mathcal{F}_{a n+1}^{pl(k)}, \\ \Delta \xi_{n+1}^{(k)} = 0, \end{cases} \quad (50)$$

where  $\chi = \Lambda_{\xi} \Omega_p - \Lambda_p \Omega_{\xi}$ .



(a) stress-strain behavior for different values of  $H_p$ .(b) evolution of  $p$  with  $H_p$ .(c) stress-strain behavior for different values of  $n_p$ .(d) evolution of  $p$  with  $n_p$ .**Fig. 5.** Influence of  $H_p$  and  $n_p$  on Fe-SMA behavior at  $T = 130^\circ\text{C}$ .

### 3.3. Tangent moduli

The implicit time-discrete integration scheme of the constitutive equations by Newton-Raphson method implies unconditional stability and quadratic convergence. However, the latter feature is ensured only by the use of consistent tangent operators. For simplicity, the consistent mechanical tangent modulus ( $\mathcal{C} = \frac{\partial \sigma}{\partial \epsilon}$ ) and consistent thermal tangent modulus ( $\mathcal{Q} = \frac{\partial \sigma}{\partial T}$ ) are replaced by the so-called *continuum tangent operators*  $\mathcal{C}$  and  $\mathcal{Q}$  given by

$$\begin{cases} \mathcal{C} = \frac{d\sigma}{d\epsilon}, \\ \mathcal{Q} = \frac{d\sigma}{dT}; \end{cases} \quad (51)$$

the expressions of which are obtained by requiring, as indicated by the consistency condition, the loading point to remain on the loading surface, i.e.  $d\mathcal{F} = 0$ . Using the multivariable chain rule for the transformation and plastic loading functions, the following system is established:

$$\begin{cases} \mathcal{F}_{\alpha,\sigma}^{\text{tr}} : d\sigma + \mathcal{F}_{\alpha,\xi}^{\text{tr}} d\xi + \mathcal{F}_{\alpha,p}^{\text{tr}} dp + \mathcal{F}_{\alpha,T}^{\text{tr}} dT = 0, \\ \mathcal{F}_{a,\sigma}^{\text{tr}} : d\sigma + \mathcal{F}_{a,\xi}^{\text{pl}} d\xi + \mathcal{F}_{a,p}^{\text{pl}} dp + \mathcal{F}_{a,T}^{\text{pl}} dT = 0. \end{cases} \quad (52)$$

Substituting  $d\sigma$  in (52) by

$$d\sigma = \mathbf{K}_{\text{eq}} : [d\epsilon - \mathbf{R}_{\xi} d\xi - \mathbf{R}_p dp], \quad (53)$$

and rearranging the factorial terms of  $d\xi$  and  $dp$ , the following new system is obtained:

$$\begin{cases} \mathcal{F}_{\alpha,\sigma}^{\text{tr}} : (\mathbf{K}_{\text{eq}} d\epsilon) + \Lambda_{\xi} d\xi + \Lambda_p dp + \mathcal{F}_{\alpha,T}^{\text{tr}} dT = 0, \\ \mathcal{F}_{a,\sigma}^{\text{pl}} : (\mathbf{K}_{\text{eq}} d\epsilon) + \Omega_{\xi} d\xi + \Omega_p dp + \mathcal{F}_{a,T}^{\text{pl}} dT = 0. \end{cases} \quad (54)$$

Solving for  $d\xi$  and  $dp$  as in the previous section, the following continuum tangent moduli are found:

- IF both inelastic mechanisms are activated, THEN solving the system gives

$$\begin{aligned} \mathcal{C}_{\text{cp}} = \mathbf{K}_{\text{eq}} &+ \left[ \frac{\Omega_p}{\chi} (\mathbf{K}_{\text{eq}} \mathbf{R}_{\xi}) - \frac{\Omega_{\xi}}{\chi} (\mathbf{K}_{\text{eq}} \mathbf{R}_p) \right] \otimes (\mathbf{K}_{\text{eq}} \mathcal{F}_{\alpha,\sigma}^{\text{tr}}) \\ &+ \left[ \frac{\Lambda_{\xi}}{\chi} (\mathbf{K}_{\text{eq}} \mathbf{R}_p) - \frac{\Lambda_p}{\chi} (\mathbf{K}_{\text{eq}} \mathbf{R}_{\xi}) \right] \otimes (\mathbf{K}_{\text{eq}} \mathcal{F}_{a,\sigma}^{\text{pl}}), \end{aligned} \quad (55)$$

$$\begin{aligned} \mathcal{Q}_{\text{cp}} = \left[ \frac{\Omega_p}{\chi} \mathcal{F}_{\alpha,T}^{\text{tr}} - \frac{\Lambda_p}{\chi} \mathcal{F}_{a,T}^{\text{pl}} \right] &(\mathbf{K}_{\text{eq}} \mathbf{R}_{\xi}) \\ &+ \left[ \frac{\Lambda_{\xi}}{\chi} \mathcal{F}_{a,T}^{\text{pl}} - \frac{\Omega_{\xi}}{\chi} \mathcal{F}_{\alpha,T}^{\text{tr}} \right] (\mathbf{K}_{\text{eq}} \mathbf{R}_p), \end{aligned} \quad (56)$$

- IF only phase transformation is activated, THEN the first equation of (54) gives

$$\begin{cases} \mathcal{C}_{\text{tr}} = \mathbf{K}_{\text{eq}} + \frac{1}{\Lambda_{\xi}} (\mathbf{K}_{\text{eq}} \mathbf{R}_{\xi}) \otimes (\mathbf{K}_{\text{eq}} \mathcal{F}_{\alpha,\sigma}^{\text{tr}}), \\ \mathcal{Q}_{\text{tr}} = \frac{1}{\Lambda_{\xi}} \mathcal{F}_{\alpha,T}^{\text{tr}} (\mathbf{K}_{\text{eq}} \mathcal{F}_{\alpha,\sigma}^{\text{tr}}), \end{cases} \quad (57)$$

- IF only plasticity is activated, THEN the second equation of (54) yields

$$\begin{cases} \mathcal{C}_{\text{pl}} = \mathbf{K}_{\text{eq}} + \frac{1}{\Omega_p} (\mathbf{K}_{\text{eq}} \mathbf{R}_p) \otimes (\mathbf{K}_{\text{eq}} \mathcal{F}_{a,\sigma}^{\text{pl}}), \\ \mathcal{Q}_{\text{pl}} = \frac{1}{\Omega_p} \mathcal{F}_{a,T}^{\text{pl}} (\mathbf{K}_{\text{eq}} \mathcal{F}_{a,\sigma}^{\text{pl}}). \end{cases} \quad (58)$$

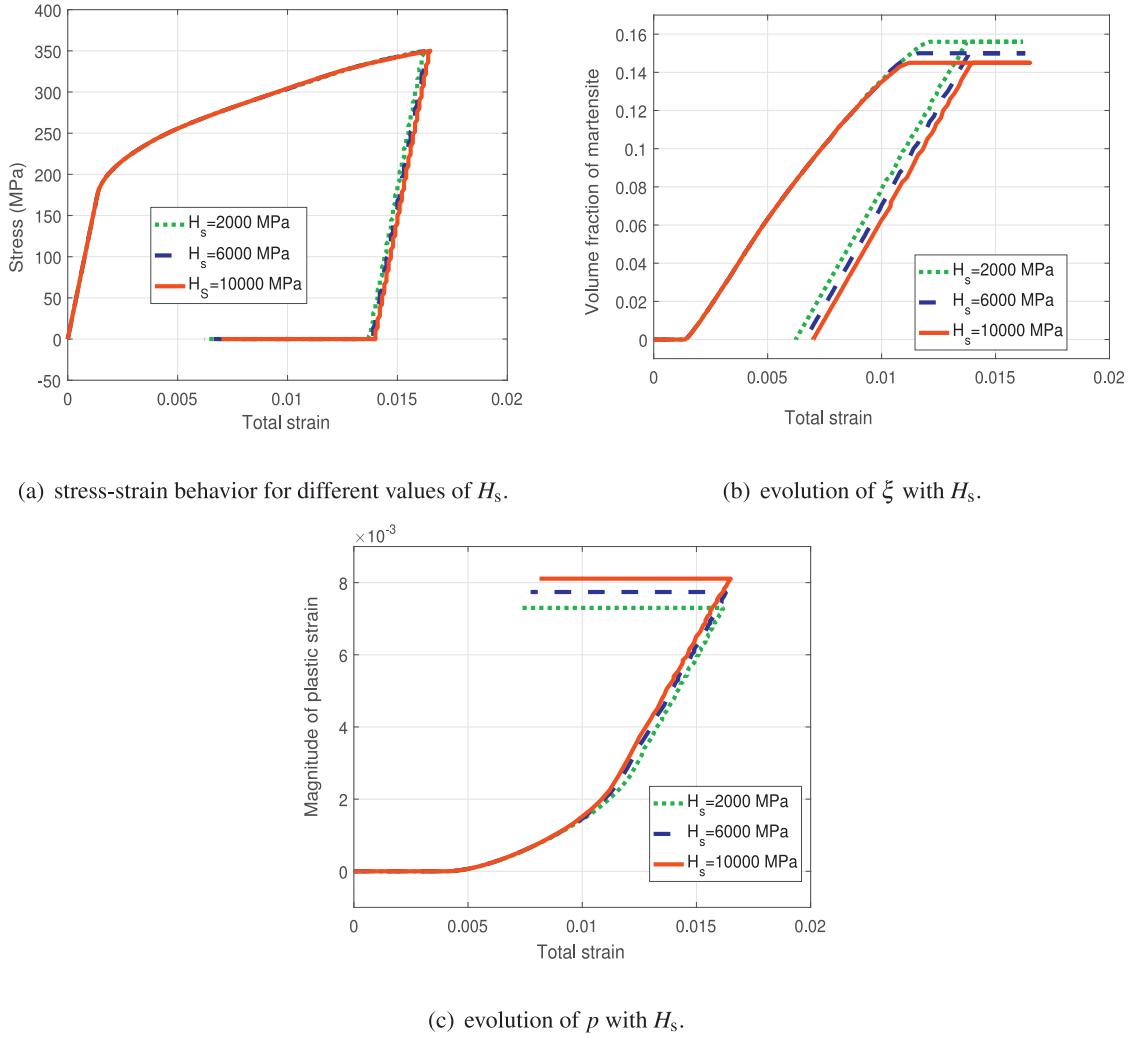


Fig. 6. Influence of  $H_s$  on Fe-SMA behavior at  $T = 50$  °C.

In the present work, the mechanical and thermal problems are not fully coupled. In other words, the thermomechanical analysis does not consider heat transfer. Therefore, the thermal tangent modulus is not needed in the simulations.

#### 4. Determination of the material parameters

The parameters of the model are calibrated using the tensile tests of Khalil et al. (2012). For this purpose, the constitutive relations are first reduced to their uniaxial formulations and the following new constants are defined

$$\hat{H}_v = \left(\frac{3}{2}\right)^{\frac{n_v+1}{2}} \varepsilon_L^{n_v+1} H_v, \quad (59)$$

$$\hat{H}_{pv} = \left(\frac{3}{2}\right)^{\frac{n_{pv}+1}{2}} \varepsilon_L^{n_{pv}+1} H_{pv}, \quad (60)$$

$$\hat{H}_p = \left(\frac{3}{2}\right)^{\frac{n_p+1}{2}} H_p. \quad (61)$$

Parameters such as the  $M_s^0$ ,  $A_s^0$ , and  $\varepsilon_L$  are taken directly from the DSC experiment and tensile tests. The remaining constants are determined by least square fitting using Matlab.

##### Step 1: fitting of the transformation parameters

The uniaxial stress-strain curves at low loading temperature ( $T = 20$  °C) where only phase transformation takes place, and moderate loading temperature ( $T = 50$  °C) where transformation precedes plasticity, are used to fit the transformation parameters.

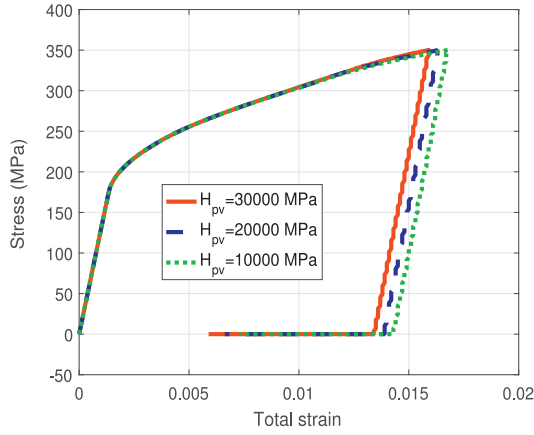
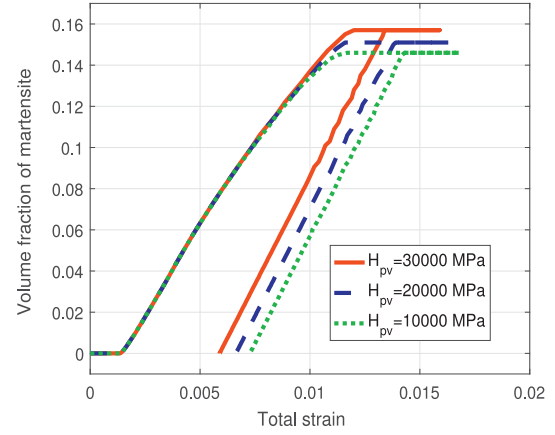
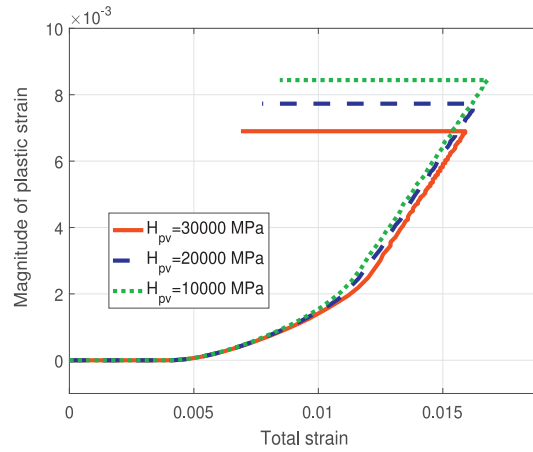
1. Parameter  $\zeta_m$  is determined from the critical transformation stresses for  $T = 20$  °C and  $T = 50$  °C. If  $B_{tr}$  is the slope of the martensite start line, consistency gives  $\zeta_m = B_{tr} \varepsilon_L$ .
2. Experiments of Nishimura et al. (1999) show that, depending on the loading conditions, the ratio  $\frac{\zeta_a}{\zeta_m}$  varies between 1.8 and 2.1 for Fe-Mn-Si SMAs. Therefore, in the present work, we set  $\zeta_a = 2\zeta_m$ .
3. In order to obtain  $\sigma_m^{tr}$ ,  $\hat{H}_v$ , and  $n_v$ , the forward transformation condition  $\mathcal{F}_m^{tr} = 0$  is written in the form  $\hat{\sigma} = f(\xi)$ , for  $T = 20$  °C, with

$$\hat{\sigma} = \frac{E_{ma}}{2} \sigma^2 + \sigma \varepsilon_L, \quad (62)$$

$$f(\xi) = \hat{H}_v \xi^{n_v} + \zeta_m (20 - M_s^0) + \sigma_m^{tr} \varepsilon_L + (\lambda_1 - \lambda_2). \quad (63)$$

The nonlinear least square curve fitting toolbox of Matlab is then used to extract the constants, based on bisquare Levenberg–Marquardt algorithm.

4. Considering the strain recovery at zero stress for  $T = 20$  °C, parameter  $\sigma_a^{tr}$  and  $H_x$  are obtained by setting

(a) stress-strain-behavior for different values of  $H_{pv}$ .(b) evolution of  $\xi$  with  $H_{pv}$ .(c) evolution of  $p$  with  $H_{pv}$ .**Fig. 7.** Influence of  $H_{pv}$  on Fe-SMA behavior at  $T = 50^\circ\text{C}$ .

$\mathcal{F}_a^{\text{tr}} = 0$  at  $T = A_s^0$  with  $\xi = 1$ , and  $\mathcal{F}_a^{\text{tr}} = 0$  at  $T = A_f^0$  with  $\xi = 0$ . It can be easily shown that  $\sigma_a^{\text{tr}} = \frac{\zeta_a}{\varepsilon_L}(A_f^0 - A_s^0)$  and  $H_x = -\hat{H}_v + \zeta_a(A_f^0 - A_s^0)$ .

### Step 2: fitting of the plasticity parameters

The uniaxial stress-strain curves at high loading temperature ( $T = 130^\circ\text{C}$ ) where only plasticity is activated, and moderate loading temperature ( $T = 50^\circ\text{C}$ ) where plasticity catches up the martensitic transformation are used to fit the gliding parameters.

1. Parameter  $\beta$  is determined as the slope of the plasticity start line, and yields, in turn, the value of  $\sigma_a^{\text{pl}}$ .
2. For  $T = 130^\circ\text{C}$ , the plasticity condition  $\mathcal{F}_a^{\text{pl}} = 0$  is written in the form  $\sigma = g(p)$ , with

$$g(p) = \hat{H}_p[p(1 - \xi)]^{n_p} + \sigma_a^{\text{pl}} - \beta T. \quad (64)$$

The nonlinear least square curve fitting toolbox of Matlab is then used to extract the values of  $\hat{H}_p$  and  $n_p$ .

### Step 3: fitting of the coupling parameters

The coupling parameters  $\hat{H}_{pv}$  and  $n_{pv}$  are obtained from stress-strain data at  $T = 50^\circ\text{C}$  where both transformation and plasticity are activated. However, accurate identification of these parameters requires to know the precise evolution of the transformation strain and plastic strain during the

loading stage. With only one stress-strain curve available, the inelastic part of the stress-strain curve is divided into a segment in which the inelastic strain is due exclusively to phase transformation, a segment in which it comes from both transformation and plasticity, and a segment in which it is yielded by only plastic deformation. The loading conditions  $\mathcal{F}_m^{\text{tr}} = 0$  and  $\mathcal{F}_a^{\text{pl}} = 0$ , are written in the second segment, respectively, as  $\hat{\sigma} = f_1(\xi, p)$  and  $\sigma = f_2(\xi, p)$ , with

$$f_1(\xi, p) = \zeta_m(T - M_s^0) + \hat{H}_v \xi^{n_v} + \hat{H}_{pv}[p(1 - \xi)]^{n_{pv}+1} \xi^{n_{pv}} + \sigma_m^{\text{tr}} \varepsilon_L - H_s p^2, \quad (65)$$

$$f_2(\xi, p) = \hat{H}_p[p(1 - \xi)]^{n_p} + \hat{H}_{pv}[p(1 - \xi)]^{n_{pv}} \xi^{n_{pv}+1} + \frac{1}{(1 - \xi)} < \sigma_0^{\text{pl}} - \beta T >. \quad (66)$$

Fitting these equations help find the values of  $\hat{H}_{pv}$ ,  $n_{pv}$  and  $H_s$ ; all other parameters being known.

The above procedure gives the parameters listed in Table 2.

## 5. Uniaxial results

The model is used to simulate the uniaxial stress-strain behavior of Fe-31.6Mn-6.45Si-0.018C (wt%) subjected to a uniaxial tensile

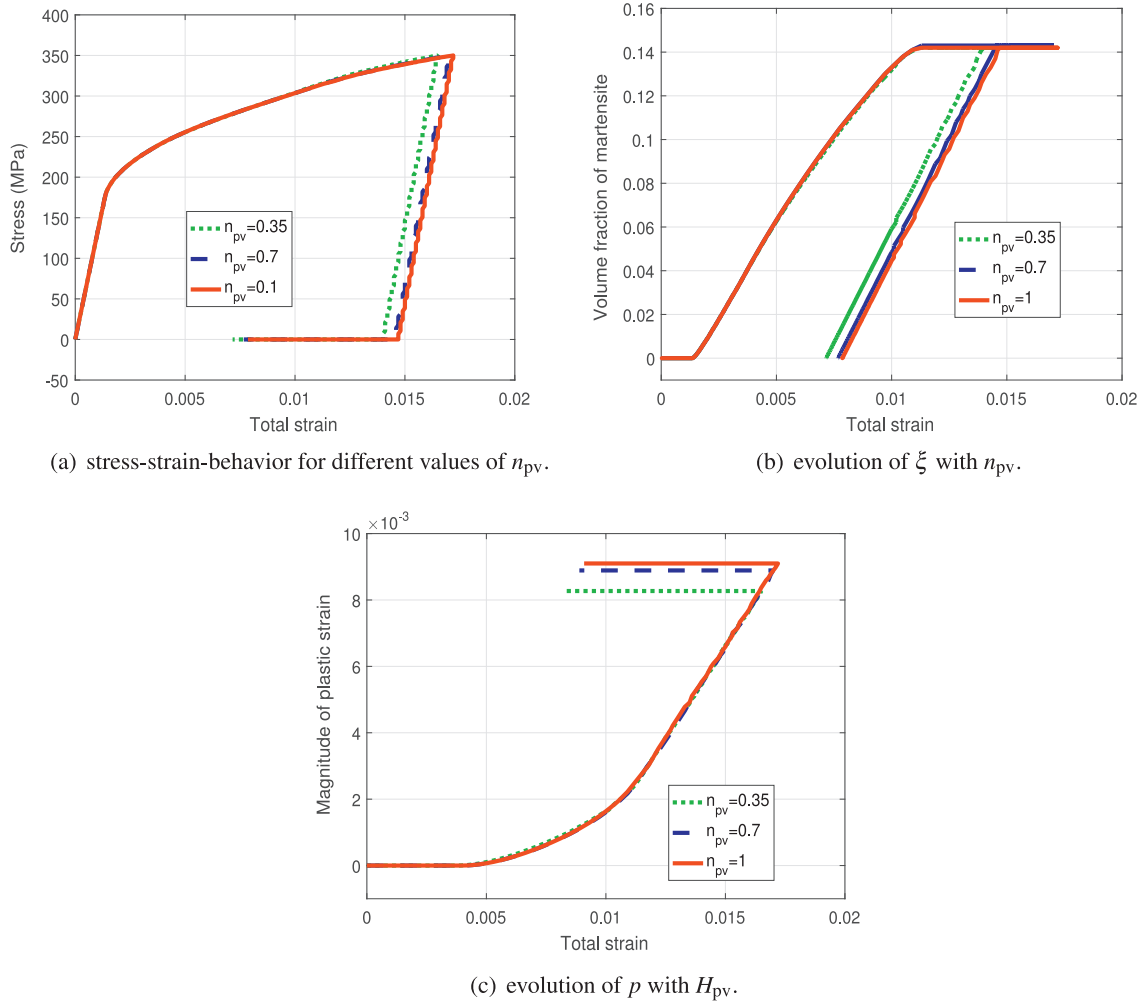


**Fig. 8.** Influence of  $H_{pv}$  and  $n_{pv}$  on Fe-SMA behavior at  $T = 50^\circ\text{C}$ .

loading cycle at different temperatures, followed by heating above  $A_f$ .

### 5.1. Validation of the model

The uniaxial results of the present model are first confronted with the experimental and numerical data of Khalil et al. (2012). Fig. 1(a) shows that both models give accurate results for low temperature ( $T = 20^\circ\text{C}$ ) where only phase transformation occurs. However at elevated temperature, ( $T = 130^\circ\text{C}$ ), the current model gives better loading prediction compared to Khalil et al. (2012) which displays a quasi-linear stress-strain loading curve (see Fig. 1(c)). This indicates an improvement in the model itself and/or a better fit of the material parameters. It is worth nothing from the strain recovery that the inelastic strain is due exclusively to phase transformation at  $T = 20^\circ\text{C}$  and only to plastic slip at  $T = 130^\circ\text{C}$ . For the crucial case of  $T = 50^\circ\text{C}$  in Fig. 1(b) where there is coupling between transformation and plasticity, our simulation result is significantly more accurate than the numerical prediction of Khalil et al. (2012); not only in terms of the nonlinearity of the loading stress-strain curve but also the recovery of the inelastic strain. Our model predicts 97% of the experimentally reported inelastic strain recovery while Khalil et al. (2012) is limited to only 33%. This may results, for example, from the use in the current model of different critical stress and slopes of transformation lines between forward and reverse phase changes and a better interaction energy. This is a significant improvement of the present

work since poor prediction of the shape memory effect will result in inaccurate design.

### 5.2. Some numerical investigations

The results in the previous section shows clearly that the current model predicts efficiently the experimental results and is more accurate than Khalil et al. (2012). The following lines will focus on the numerical investigations of some important aspects of Fe-Mn-Si.

#### 5.2.1. Competition between transformation and plasticity

Because plastic deformation interferes with martensite transformation in Fe-Mn-Si, the increase of the plastic yield strength of austenite with decreasing temperature allows improved recovery of inelastic strain at low loading temperatures. Fig. 2(a) gives the stress-strain-temperature behavior of the material for different loading temperatures  $T_{\text{exp}}$ . Evolutions of these state variables highlight a nonlinear recovery of the inelastic strain during reverse transformation by heating. This recovery of the inelastic strain was found to decrease when the loading temperature is augmented. This latter feature is depicted more clearly in Fig. 2(b), where the ratio of the transformation strain over the total inelastic strain is shown to evolve in an inverse sigmoid relationship with  $T$ . A possible explanation is that while both phase transformation and plastic yielding occur by shearing, the energy of Shockley partial dislocations in presence of martensite transformation may become lower

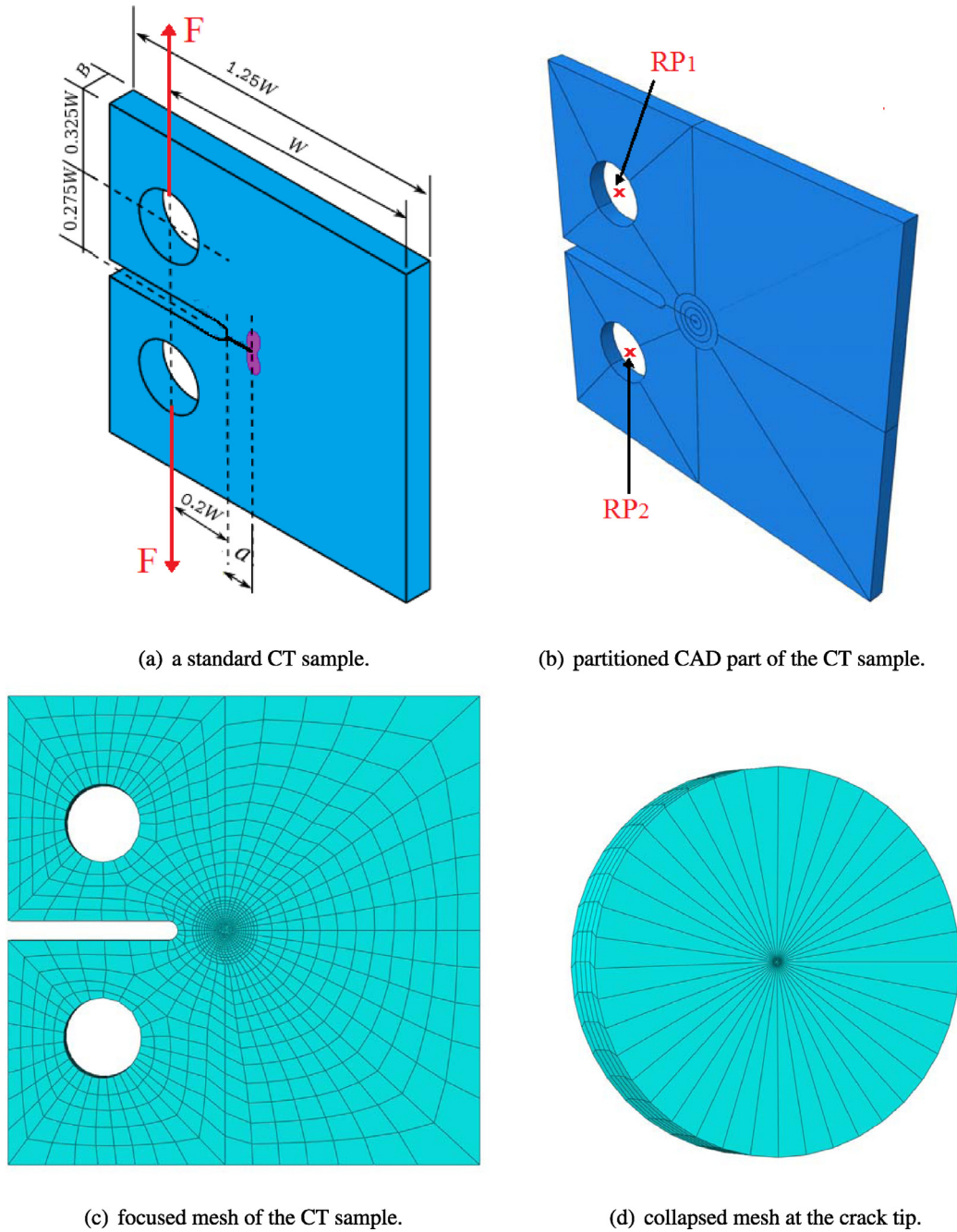


Fig. 9. Design of the 3D CT sample.

than that of plastic dislocation as the temperature decreases. The large temperature range [40 °C, 100 °C] within which the coupling occurs, raises the importance of having a model that predicts accurately the SME in presence of plastic deformation.

### 5.2.2. Simulation of partial unloading

To simulate partial unloadings, the material is loaded up to 350 MPa at constant temperatures  $T = 20$  °C for Fig. 3(a) and  $T = 50$  °C for Fig. 3(b), followed by unloading to  $\sigma_u = 100$  MPa and  $\sigma_u = 50$  MPa. Heating is then operated at these constant hold stresses. The results show that the initial shape is not fully recovered even in absence of plastic deformation. This is especially the case for  $T = 20$  °C where the closure point of the loop highlights residual elastic strain. For  $T = 50$  °C, it can also be seen that the strain value at the end of the heating stage decreases as the hold

stress increases; corresponding to an augmentation of the residual elastic strain.

### 5.2.3. Influence of $H_v$ and $n_v$

The influences of these parameters are investigated at low temperature ( $T = 20$  °C) for which phase transformation is the only dissipative mechanism. In Fig. 4(a), it can be seen that higher values of  $H_v$  results in steeper stress-strain curve during forward transformation. In fact,  $H_v$  expresses the resistance of the material to further phase transformation, which translates into lower martensite volume fraction as  $H_v$  increases (see in Fig. 4(b)). Similar analysis using parameter  $n_v$  indicates higher nonlinearity with increasing  $n_v$  as shown in Fig. 4(c). This is especially noticeable at the beginning of phase transformation where higher values of  $n_v$  result in more pronounced curvature of the stress-strain plot. The



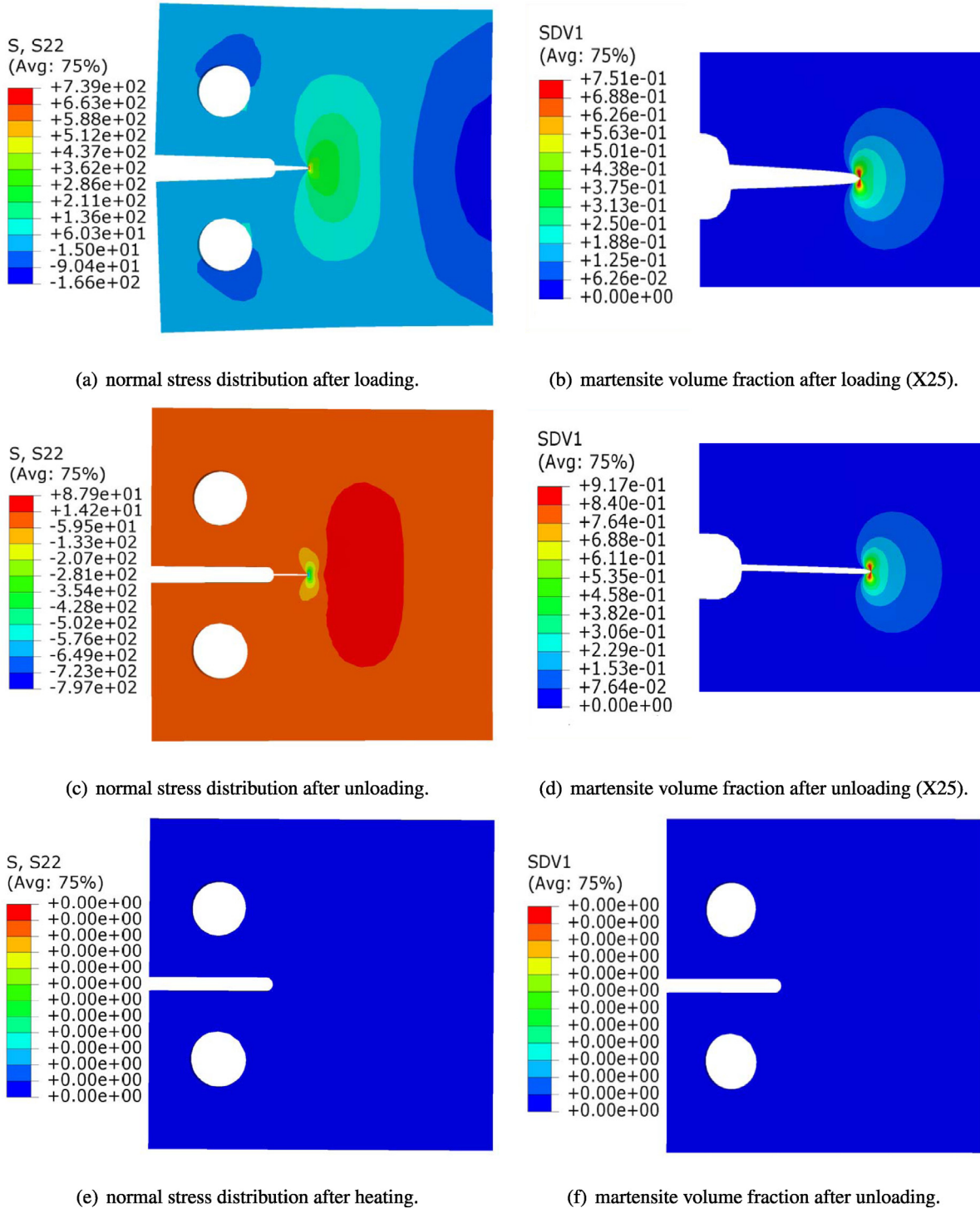


Fig. 10. Distributions of stress and strain in the specimen under plane stress conditions at  $T = 20\text{ }^{\circ}\text{C}$ .

observed hardening becomes increasingly linear as  $n_v$  approaches 1. However, in contrast to  $H_v$ , the martensite volume fraction augments as  $n_v$  increases, thus amounting to lower hardening (see Fig. 4(d)).

#### 5.2.4. Influence of $H_p$ and $n_p$

The effects of these parameters are studied at high temperature ( $T = 135\text{ }^{\circ}\text{C}$ ) where only plasticity is activated. As shown in Fig. 5, the influence of  $H_p$  and  $n_p$  on the evolution of plastic strain and the overall stress-strain behavior at elevated temperature are

similar to those observed for  $H_v$  and  $n_v$  at low temperature for  $\xi$ . It does appear, however, from comparing Figs. 5 and 4, that the model is more sensitive to variations in  $H_v$  than  $H_p$ .

#### 5.2.5. Influence of $H_s$

Parameter  $H_s$  accounts for the effects of the plastic slip in the activation of direct transformation. Fig. 6 shows that variation in the values of  $H_s$  does not alter the general trend of the stress-strain curves except the final values of the strains reached at the end of the loading stage. This can be noticed more clearly in Fig. 6(b)

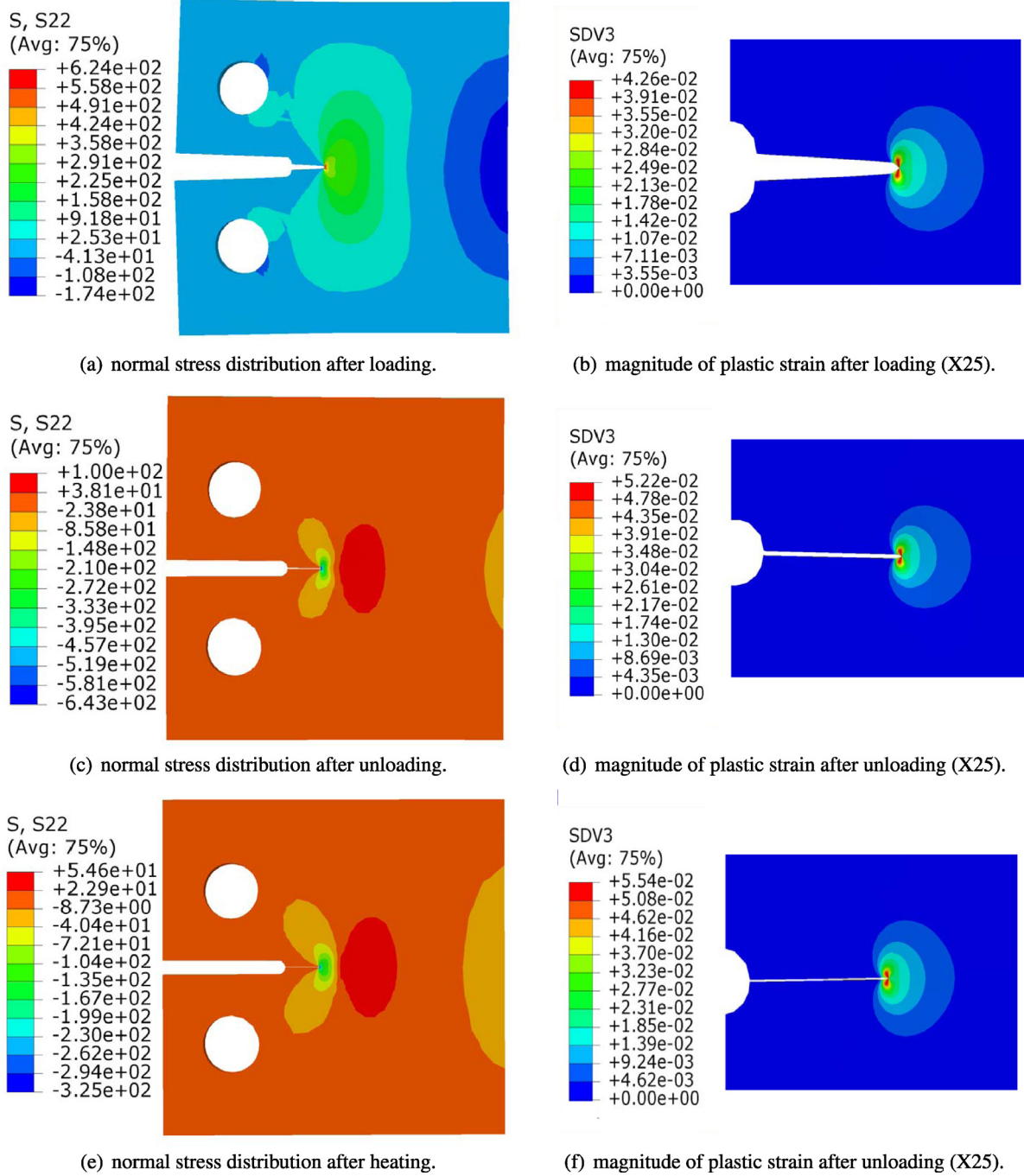


Fig. 11. Distributions of stress and strain in the specimen under plane stress conditions at  $T = 120\text{ }^{\circ}\text{C}$ .

and (c) where higher values of  $H_s$  correspond to lower martensite volume fraction and higher magnitude of plastic strain. This meets theoretical expectation since the greater is the value of  $H_s$  the more severe is the retardation or deceleration effects of the plasticity on the transformation mechanism. One can see that for strain values between 0.5% and 1.1% the production of martensite decreases while plastic slippage increases, while above the critical strain value of 1.1%, only plasticity is activated.

### 5.2.6. Influence of $H_{pv}$ and $n_{pv}$

Parameter  $H_{pv}$  and  $n_{pv}$  accounts for interaction between grains and between martensite variants and plastic slip systems. The simulation results in Figs. 7 and 8 show similar trend than for  $H_s$  ex-

cept that the model is not very sensitive to  $n_{pv}$ , and inverse effects are observed for  $H_{pv}$ . Equations (65) and (66) point out that the alteration (related to  $H_{pv}$  and  $n_{pv}$ ) induced by plastic slip on phase change is  $\frac{p(1-\xi)}{\xi}$  times the effect of transformation on plasticity. Considering the orders of magnitude of  $p$  and  $\xi$ , one can easily understand the results. It should be noted that the nonlinearity of the stress-strain curves when  $n_{pv} = 1$  is related to the other coefficients,  $n_v$  and  $n_p$ .

## 6. Finite element analysis of a 3D compact tension sample

The 3D formulation of the model aims at developing a simulation tool for the design of Fe-SMAs engineering structures.

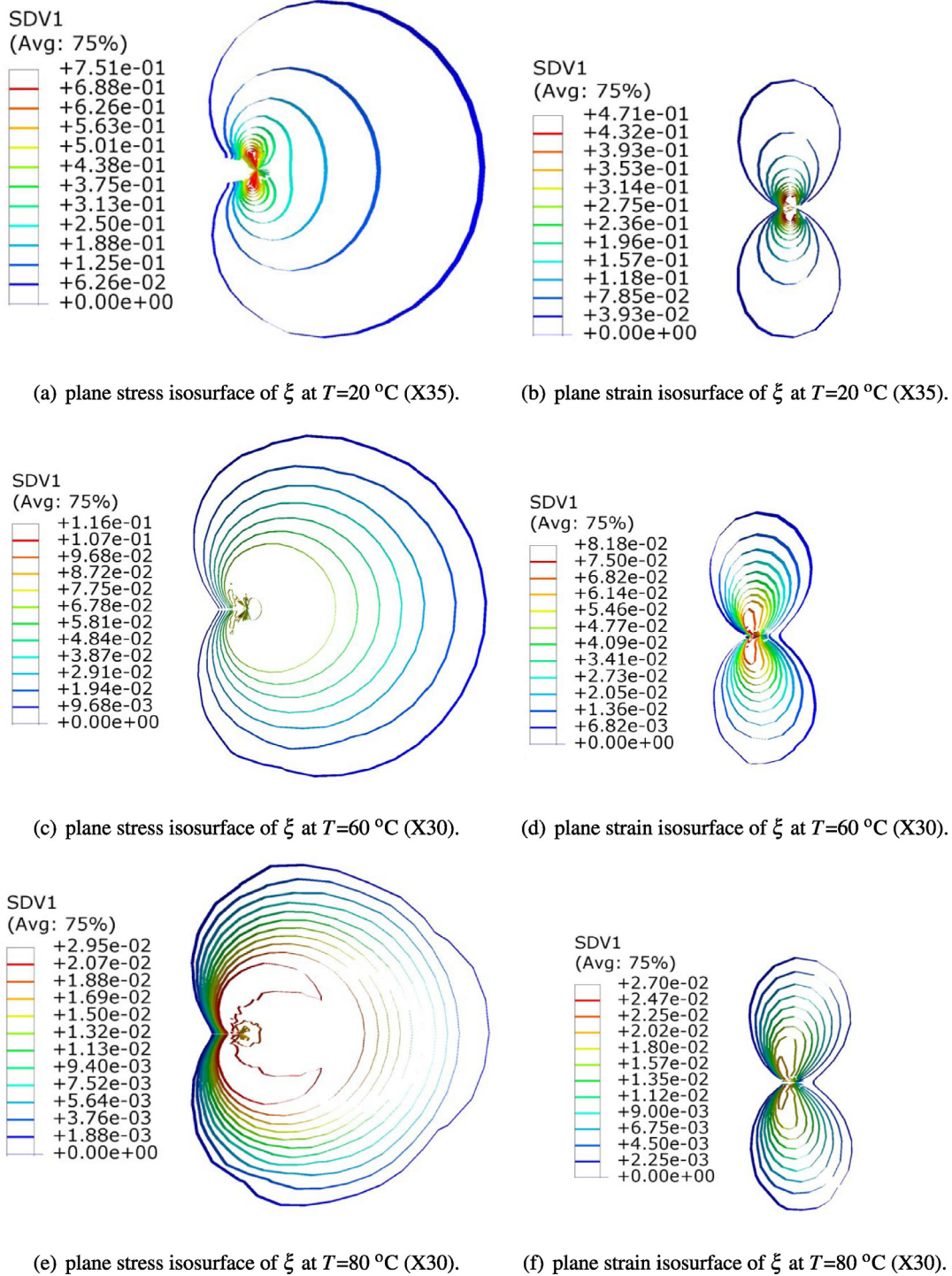


Fig. 12. Isosurfaces of transformation zones near the crack tip: plane stress vs. plane strain.

A common approach in computational mechanics is to integrate the model in a “finite element method”-based software such as ABAQUS. To this end, the constitutive equations are implemented in a user defined material subroutine (UMAT). In the present paper, we assume a homogeneous distribution of the temperature inside the material. Therefore, for a given thermomechanical loading path, the process starts by applying the mechanical load, the thermal predefined field and the specific boundary conditions. From the boundary conditions and load increments, the global solver finds deformation guesses for the nodes by constructing a global stiffness matrix based on the elastic behavior of the material. The

obtained local total strains, together with the values of the internal variables, are used in the UMAT to calculate the local stresses and the local tangent stiffnesses. The way how the increment of internal variables are computed is detailed in Section 3.1. After convergence of the implicit and iterative integration process, the final stress values are used to compute the forces acting at each node. Static equilibrium is then checked, by requiring the magnitude of the residual force, i.e. the sum of the force vectors, to be less than a tolerance value. If it fails, the “Newton–Raphson” method is used by the global server to find new guesses for the global deformations from the global tangent stiffness matrix. In the following sec-



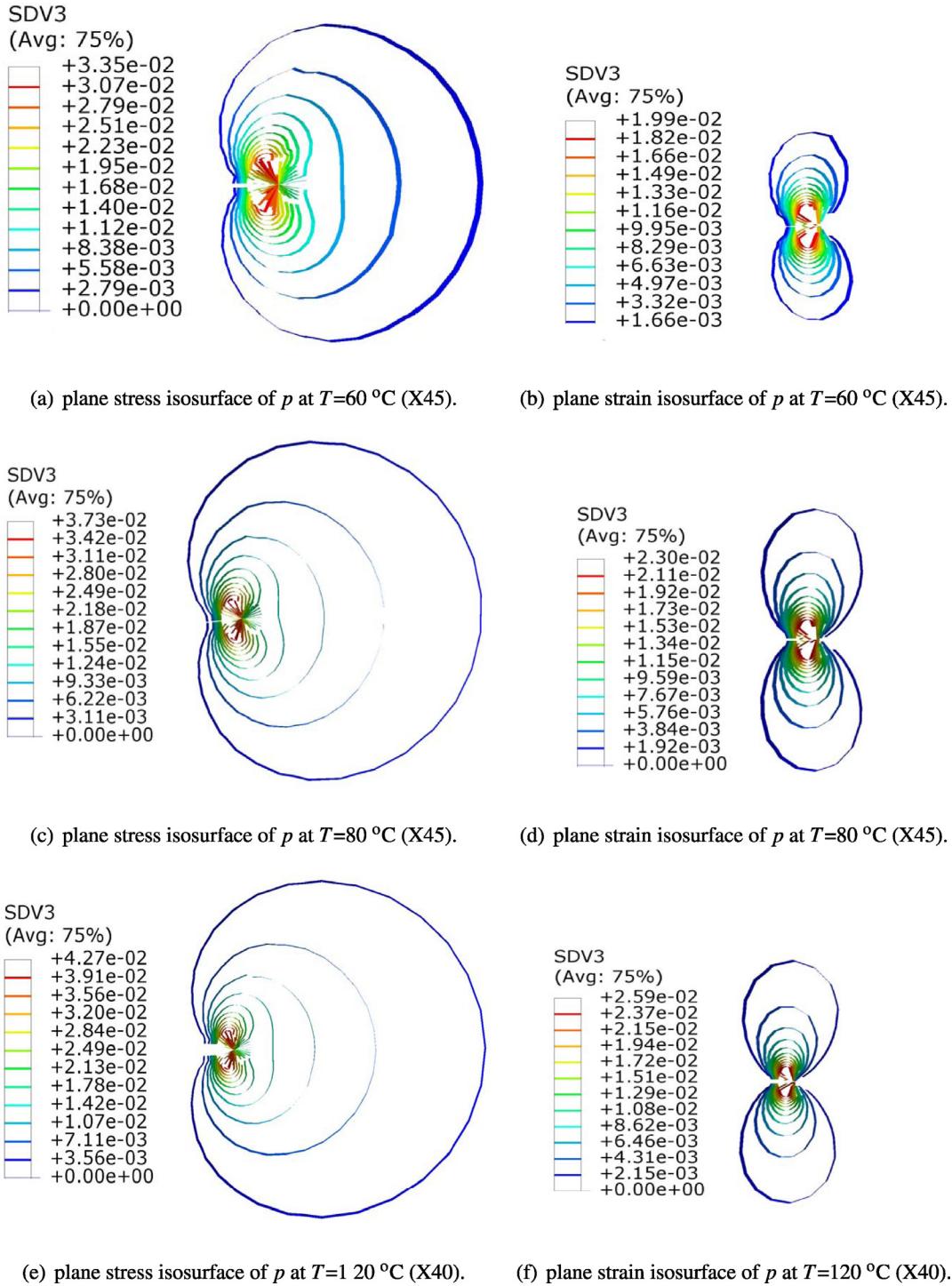


Fig. 13. Isosurfaces of plastic zones near the crack tip: plane stress vs. plane strain.

tions, the above procedure is used to show the capability of the model to forecast the behavior of 3D structures with highly heterogeneous distributions of stress and strain under complex thermo-mechanical loading path. A typical case is the precracked compact tension sample (CT sample) under mode I loading.

#### 6.1. Design of the CT sample

Fig. 9(a) gives the standard dimensions of a CT sample. In this study, we use a reference length  $W = 20\text{ mm}$ , a pre-crack length  $a = W/8$  and thickness  $B = W/20$ . The partitioned geometry of the

CT sample is presented in Fig. 9(b). The geometry was partitioned in order to generate a structured and efficient mesh as illustrated in Fig. 9(c). The pins that transmit the load of the clevises to the specimen are represented by rigid bodies corresponding to reference points RP1 and RP2. The *interaction module* of ABAQUS was used to couple the RPs with the corresponding half hole surfaces, and to specify the crack front, seam and propagation direction. The crack seam corresponds to a face that is originally closed but can open during the analysis thanks to a duplication of its mesh nodes. It is well known from fracture mechanics that strain singularity develops at crack tips. However, the nature of the material dictates

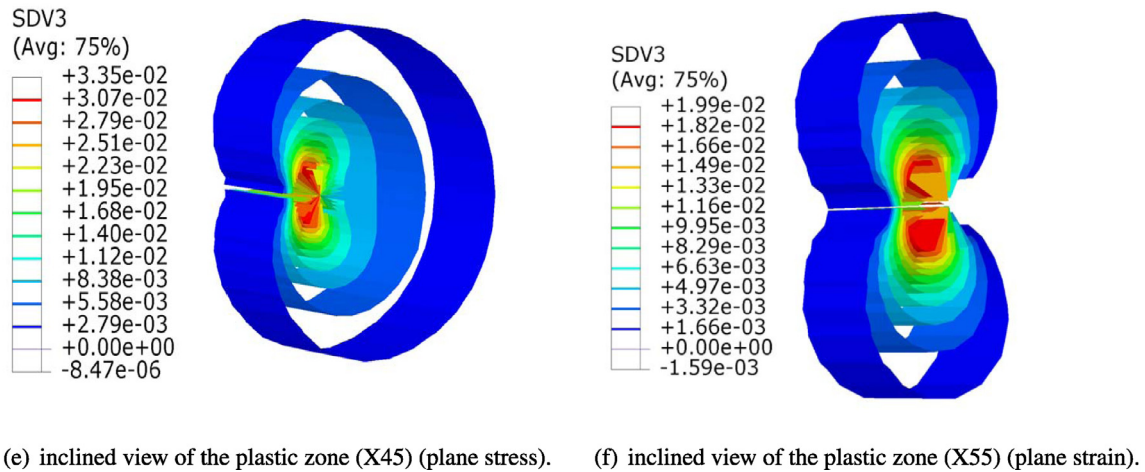
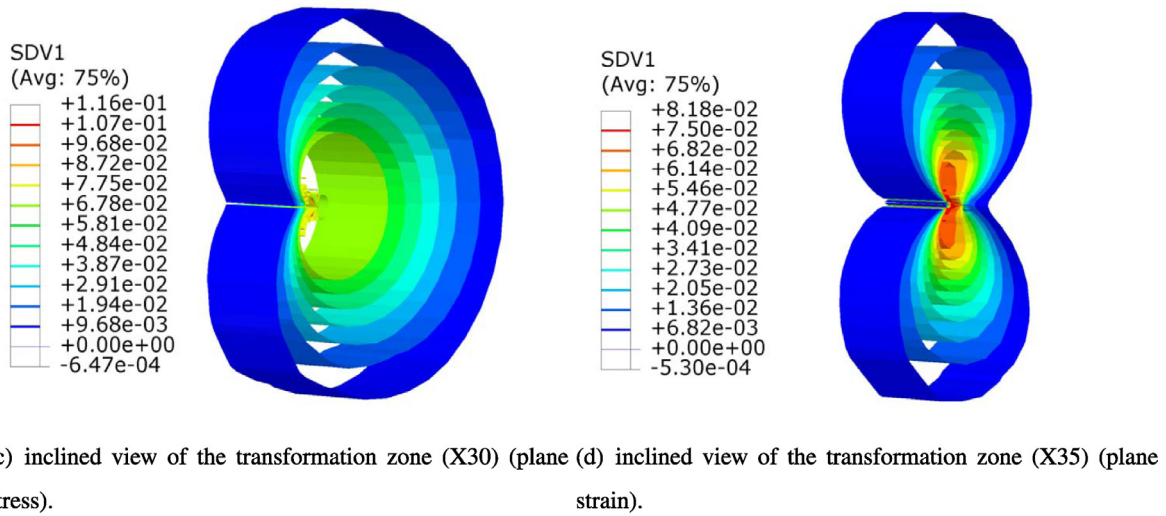
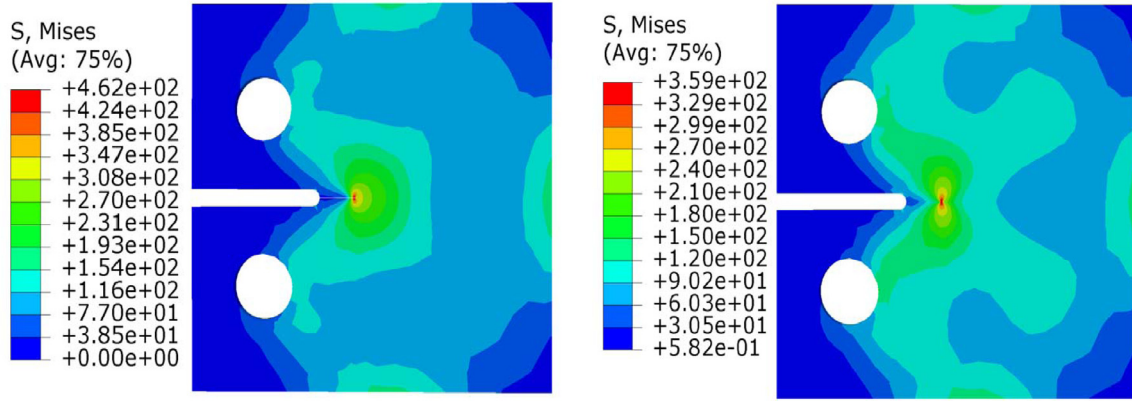


Fig. 14. Distributions of stress and strain in the specimen under plane stress conditions at  $T = 60$  °C.

the singularity type. For instance, linear elastic materials present  $1/\sqrt{r}$  strain singularity at sharp crack tips, perfectly plastic materials show  $1/r$  strain singularity, whereas the strain singularity of hardening materials such as the studied Fe-SMAs is somewhere in between. In order to describe correctly the singularity, the crack tip is meshed using a ring of collapsed elements with a midside node parameter of 0.25. The first circular partitioned area around the crack tip is swept meshed with C3D6 triangular prism wedge

elements as shown in Fig. 9(d). The remaining section parts are swept meshed with C3D8 hexaedral brick elements using medial axis algorithm.

## 6.2. Numerical results and discussions

The results were obtained by applying, in Mode I, concentrated forces of magnitude 600 N at RP1 and RP2. The specimen was then unloaded and heated above  $A_f$ . The highly heterogeneous



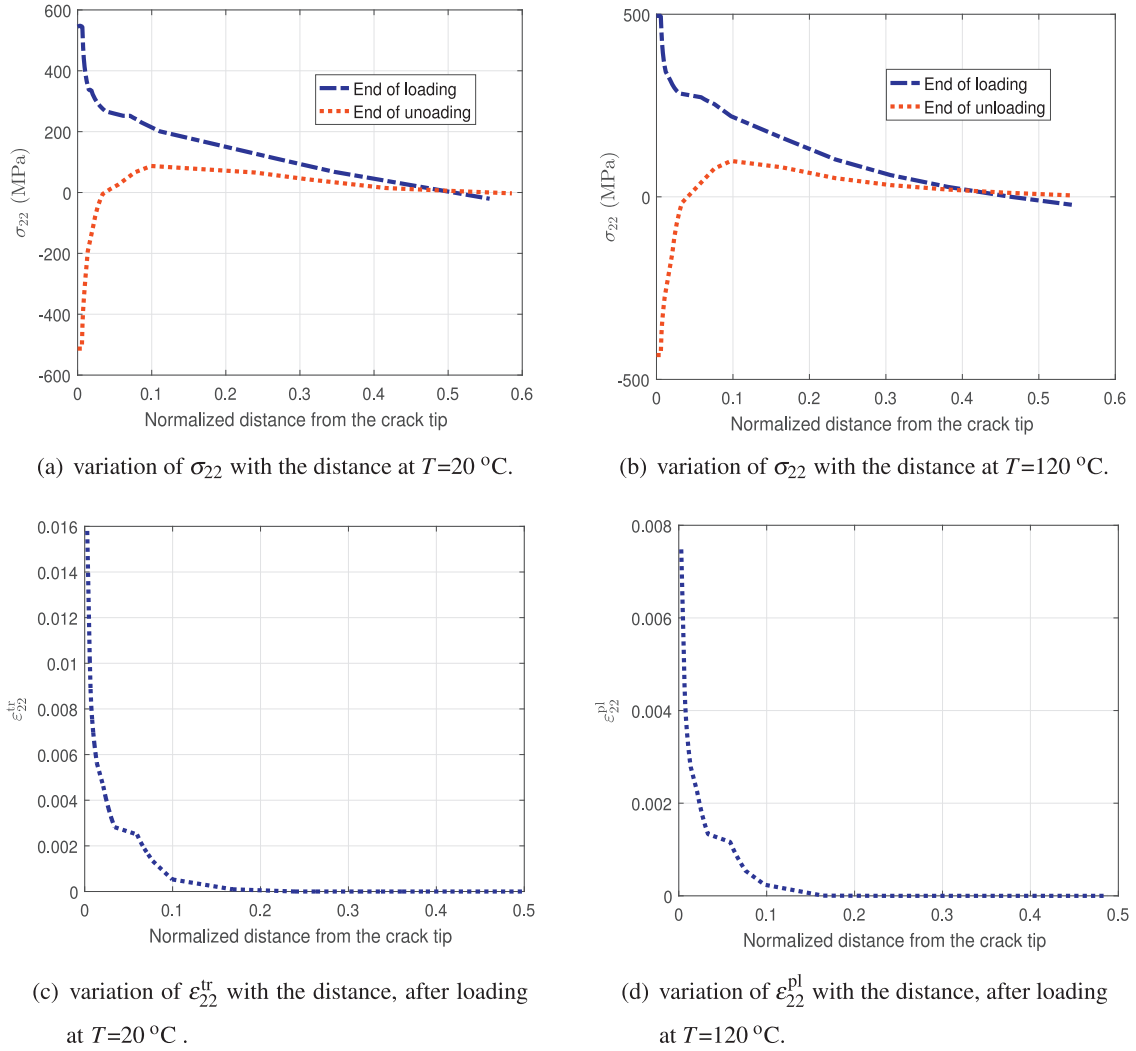


Fig. 15. variation of the normal components of stress and inelastic strains with the distance.

stress distribution as well as the development of inelastic strain singularities at the crack tip are shown in Figs. 10 and 11. As predicted by the uniaxial results, only phase transformation occurred at low temperature, only plasticity was activated at elevated temperature, and the two mechanisms were competing at intermediate temperatures. Fig. 10 shows, for the loading stage, a high tensile stress concentration (up to 739 MPa) at the crack front, and a compressive stress distribution near the specimen face opposite to the crack. This resulted in maximum volume fractions of tensile-induced and compressive-induced martensites of  $7.51 \times 10^{-1}$  and  $6.24 \times 10^{-4}$ , respectively. During unloading, a maximum compressive stress of -797 MPa was reported at the crack front, as a consequence of the non-recovery of the initial shape during unloading. This helped building compressive-induced martensite at the crack front. However, assuming a symmetric behavior, the stress reversal at the crack front induces phase change only for twice the value of the critical transformation stress. This explains the low amount of compressive-induced martensite at the crack front, which is 22.5% the value of the tensile-induced one during loading. This cyclic phase transformation reminds, in many ways, the reversed plasticity discussed in Wolf (1970), Louat et al. (1993), Donald and Paris (1999), Kujawski (2001) and Alizadeh et al. (2007). It is worth pointing out that this reversed phase transformation led to a partial but noticeable closure of the crack. The crack closure became complete only at the end of the heating process where the  $M \rightarrow A$

transformation suppresses all stress concentration and strain singularity. Therefore, the SME property of the alloy can be used for the self-healing of precracked Fe-SMA structures.

Fig. 11 points out similar results at high temperature ( $T = 120^\circ\text{C}$ ) where only plasticity was activated. However, in opposite to the phase transformation case, stress concentration was still visible at the end of the heating stage, due to the irreversibility of plastic strain. Nonetheless, the mechanical unloading generated reversed plasticity in order to accommodate the compatibility requirements between the plastic zone and the surrounding elastic region. Compared to the loading stage, the magnitude of the plastic strain increased by 22.5% after unloading and by 30.1% after heating. The increase of the plastic slip during heating shows the capability of the model to capture thermal-induced plasticity. This mechanism which is related to the linear decrease of the yield stress with increasing temperature engendered additional crack closure.

The difference between plane stress and plane strain conditions was also investigated for the fracture behavior of the specimen. Plane stress conditions were mimicked by fixing the anti-plane rigid body mode on the two sides of the panel, while plane strain conditions were obtained by restraining the anti-plane displacements. Figs. 12 and 13 give, respectively, the isosurfaces for the volume fraction of martensite and magnitude of plastic strain. A qualitative comparison of the contours shows cardioid-like shapes

for plane stress and lemniscate-like shapes for plane strain with larger transformation and plastic zones, and higher inelastic strain values for the first one. From these results, we can conclude that the fracture of this Fe-SMA would be brittle at room temperature and ductile at high temperature.

For moderate temperature ( $T = 60\text{ }^{\circ}\text{C}$ ), Fig. 14 gives the von Mises stress distribution at the end of the loading stage as well as inclined views of the transformation and plastic zones, for both plane stress and plane strain conditions. The zoom amount indicates that, for this precise temperature, the transformation zone is larger than the plastic region. Here again, plane stress gives higher values of stress and inelastic strains than plane strain.

Finally, the distribution of the stress, transformation strain and plastic strain in the loading direction are plotted against the distance from the crack tip in Fig. 15. The results show for  $T = 20\text{ }^{\circ}\text{C}$  and  $T = 120\text{ }^{\circ}\text{C}$  that these quantities decrease with the distance in a qualitatively consistent way with nonlinear fracture mechanics results.

## 7. Conclusion

In this paper, a nonlinear 3D model was proposed for Fe-SMAs. It takes into account the competition between phase transformation and plastic slip and considers different thermomechanical properties for austenite and martensite. The constitutive equations were derived from a Helmholtz free energy potential consisting of local phase energies, a new interaction energy density that takes into account the effect of the orientation, and a constraints potential that accounts for restrictions on the volume fraction of martensite using Lagrange multipliers. The integration of the time-discrete equations was accomplished using an implicit algorithm, in which the detection of active loading surfaces and the implementation of appropriate consistency conditions are inspired from computational multisurface plasticity. A specific procedure for characterizing the parameters of the model is used to determine a reference set of parameters and carry out experimental validation using stress-strain-temperature data from Khalil et al. (2012). Compared to the work of Khalil et al. (2012), the simulations show improved accuracy, especially at intermediate temperature where pronounced coupling between phase transformation and plasticity is observed. In such case, the present work predicts 97% of shape recovery contrary to Khalil et al. (2012) where it is about 33%. Finally, the model was used to simulate the thermomechanical response of a compact tension sample. The results point out, as in the uniaxial case, that the lower the loading temperature the higher the phase transformation, and the higher the loading temperature the higher the plastic deformation. The model was able to capture cyclic plasticity and martensitic transformation during unloading, thermal-induced plasticity during heating, as well as the related crack closure. The stress and inelastic strains in the loading direction were plotted as functions of the distance from the crack tip. The figures show qualitative agreement with nonlinear fracture mechanics. The obtained results demonstrate the capability of the present model to design properly Fe-SMA devices. Robustness of the present model and algorithm may be tested in more complicated cases with, for instance, surface-to-surface contacts.

## Acknowledgment

The authors would like to acknowledge the financial support of Khalifa University through KUIRF fund no. 21031.

## References

Alizadeh, H., Hills, D., De Matos, P., Nowell, D., Pavier, M., Paynter, R., Smith, D., Simandjuntak, S., 2007. A comparison of two and three-dimensional analyses of fatigue crack closure. *Int. J. Fatigue* 29 (2), 222–231.

Araki, Y., Maekawa, N., Omori, T., Sutou, Y., Kainuma, R., Ishida, K., 2012. Rate-dependent response of superelastic Cu–Al–Mn alloy rods to tensile cyclic loads. *Smart Mater. Struct.* 21 (3), 032002.

Araya, R., Marivil, M., Mir, C., Moroni, O., Sepúlveda, A., 2008. Temperature and grain size effects on the behavior of Cu–Al–Mn SMA wires under cyclic loading. *Mater. Sci. Eng.* 496 (1), 209–213.

Bansiddhi, A., Sargeant, T., Stupp, S., Dunand, D., 2008. Porous NiTi for bone implants: a review. *Acta Biomater.* 4 (4), 773–782.

Baruj, A., Troiani, H., 2008. The effect of pre-rolling Fe–Mn–Si-based shape memory alloys: mechanical properties and transmission electron microscopy examination. *Mater. Sci. Eng.* 481, 574–577.

Buehler, W.J., Cross, W.B., 1969. 55-Nitinol unique wire alloy with a memory. *Wire J.* 2 (6), 41–49.

Buehler, W.J., Gilfrich, J., Wiley, R., 1963. Effect of low-temperature phase changes on the mechanical properties of alloys near composition  $\text{TiNi}$ . *J. Appl. Phys.* 34 (5), 1475–1477.

Casciati, F., Casciati, S., Faravelli, L., 2007. Fatigue characterization of a Cu-based shape memory alloy. In: *Proceedings of the Estonian Academy of Sciences. Physics, Mathematics*, 56. Estonian Academy Publishers, pp. 207–217.

Chang, L., Read, T., 1951. Plastic deformation and diffusionless phase changes in metals—the gold-cadmium beta-phase. *Transactions of the American Institute of Mining and Metallurgical Engineers* 191 (1), 47–52.

Cissé, C., Zaki, W., Ben Zineb, T., 2016. A review of constitutive models and modeling techniques for shape memory alloys. *Int. J. Plast.* 76, 244–284.

Cissé, C., Zaki, W., Zineb, T.B., 2015. A model for iron-based shape memory alloys considering variable elastic stiffness and coupling between plasticity and phase transformation. In: *ASME 2015 Conference on Smart Materials, Adaptive Structures and Intelligent Systems*. American Society of Mechanical Engineers, V001T03A012–V001T03A012.

Cissé, C., Zaki, W., Zineb, T.B., 2016. A review of modeling techniques for advanced effects in shape memory alloy behavior. *Smart Mater. Struct.* 25 (10), 103001.

Cladera, A., Weber, B., Leinenbach, C., Czaderski, C., Shahverdi, M., Motavalli, M., 2014. Iron-based shape memory alloys for civil engineering structures: an overview. *Constr. Build. Mater.* 63 (0), 281–293.

Donald, K., Paris, P.C., 1999. An evaluation of  $\delta K$  eff estimation procedures on 6061-t6 and 2024-t3 aluminum alloys. *Int. J. Fatigue* 21, S47–S57.

Druker, A., Perotti, A., Baruj, A., Malarria, J., 2011. Heat treatments of Fe–Mn–Si based alloys: mechanical properties and related shape memory phenomena. *J. ASTM Int.* 8 (4), 1–8.

Es-Souni, M., Es-Souni, M., Fischer-Brandies, H., 2005. Assessing the biocompatibility of nitinol shape memory alloys used for medical applications. *Anal. Bioanal. Chem.* 381 (3), 557–567.

Evard, M.E., Volkov, A.A., Belyaev, F.S., Ignatova, A.D., Volkova, N.A., 2016. Microstructural modelling of plastic deformation and defects accumulation in Fe–Mn–Si based shape memory alloys. *Procedia Struct. Integr.* 2, 1546–1552. 21st European Conference on Fracture, ECF21, 20–24 June 2016, Catania, Italy.

Federzoni, L., Guenin, G., Mantel, M., 1993. Improvement of the shape memory effect of a Fe–Mn–Cr–Si–Ni by original thermomechanical treatments. *J. Phys. IV* 3 (C7), 557–560.

Frémond, M., 2002. *Non-smooth thermomechanics*. Springer.

Goluboroda, I., Rusinko, K., Tanaka, K., 1999. Description of an Fe-based shape memory alloy thermomechanical behavior in terms of the synthetic model. *Comput. Mater. Sci.* 13 (4), 218–226.

Gu, X., Zaki, W., Morin, C., Mounni, Z., Zhang, W., 2015. Time integration and assessment of a model for shape memory alloys considering multiaxial nonproportional loading cases. *Int. J. Solids Struct.* 54, 82–99.

Halphen, B., Nguyen, Q., 1974. Plastic and visco-plastic materials with generalized potential. *Mech. Res. Commun.* 1 (1), 43–47.

Jalaeefar, A., Asgarian, B., 2013. Experimental investigation of mechanical properties of nitinol, structural steel, and their hybrid component. *J. Mater. civil Eng.* 25 (10), 1498–1505.

Jemal, F., Bouraoui, T., Ben Zineb, T., Patoor, E., Bradaï, C., 2009. Modelling of martensitic transformation and plastic slip effects on the thermo-mechanical behaviour of Fe-based shape memory alloys. *Mech. Mater.* 41 (7), 849–856.

Johnson, A. D., 2013. Biocompatible copper-based single-crystal shape memory alloys. US Patent 8,556,969.

Kajiwar, S., 1999. Characteristic features of shape memory effect and related transformation behavior in Fe-based alloys. *Mater. Sci. Eng.* 273, 67–88.

Kajiwar, S., Liu, D., Kikuchi, T., Shinya, N., 2001. Remarkable improvement of shape memory effect in Fe–Mn–Si based shape memory alloys by producing NbC precipitates. *Scr. Mater.* 44 (12), 2809–2814.

Khalil, W., Mikolajczak, A., Bouby, C., Ben Zineb, T., 2012. A constitutive model for Fe-based shape memory alloy considering martensitic transformation and plastic sliding coupling: application to a finite element structural analysis. *J. Intell. Mater. Syst. Struct.* 23, 1143–1160.

Khalil, W., Saint-Sulpice, L., Arbab Chirani, S., Bouby, C., Mikolajczak, A., Ben Zineb, T., 2013. Experimental analysis of Fe-based shape memory alloy behavior under thermomechanical cyclic loading. *Mech. Mater.* 63, 1–11.

Kujawski, D., 2001. Enhanced model of partial crack closure for correlation of r-ratio effects in aluminum alloys. *Int. J. Fatigue* 23 (2), 95–102.

Lazghab, T., Wu, K., 2005. One-dimensional shape memory alloy model with plastic deformation effects. *ICOMAT14–17th June*.

Lin, K.-M., Chen, J.-H., Lin, C.-C., Liu, C.-H., Lin, H.-C., 2014. Optimization of shape-memory effect in Fe–Mn–Si–Cr–Re shape-memory alloys. *J. Mater. Eng. Perform.* 23, 2327–2332.

- Louat, N., Sadananda, K., Duesbery, M., Vasudevan, A., 1993. A theoretical evaluation of crack closure. *Metall. Trans. A* 24 (10), 2225–2232.
- Miyazaki, S., Mizukoshi, K., Ueki, T., Sakuma, T., Liu, Y., 1999. Fatigue life of Ti–50at.%Ni and Ti–40Ni–10Cu (at.%) shape memory alloy wires. *Mater. Sci. Eng.* 273, 658–663.
- Moumni, Z., Zaki, W., Nguyen, Q.S., 2008. Theoretical and numerical modeling of solid–solid phase change: application to the description of the thermomechanical behavior of shape memory alloys. *Int. J. Plast.* 24 (4), 614–645.
- Niitsu, K., Omori, T., Kainuma, R., 2011. Superelasticity at low temperatures in Cu–17Al–15Mn (at.%) shape memory alloy. *Mater. Trans.* 52 (8), 1713–1715.
- Nishimura, F., Liedl, U., Werner, E., 2003. Simulation of martensitic transformations in TRIP-steel and Fe-based shape memory alloy. *Comput. Mater. Sci.* 26, 189–196.
- Nishimura, F., Watanabe, N., Tanaka, K., 1997. Analysis of uniaxial stress-strain-temperature hysteresis in an Fe-based shape memory alloy under thermomechanical loading. *Comput. Mater. Sci.* 8 (4), 349–362.
- Nishimura, F., Watanabe, N., Watanabe, T., Tanaka, K., 1999. Transformation conditions in an Fe-based shape memory alloy under tensile–torsional loads: martensite start surface and austenite start/finish planes. *Mater. Sci. Eng.* 264 (1), 232–244.
- Olson, G., Cohen, M., 1982. Stress-assisted isothermal martensitic transformation: application to trip steels. *Metall. Trans. A* 13 (11), 1907–1914.
- Otsuka, H., 1991. Fe–Mn–Si based shape memory alloys. In: *MRS Proceedings*, 246. Cambridge University Press, p. 309.
- Otsuka, K., Wayman, C.M., 1999. *Shape memory materials*. Cambridge university press.
- Ould Moussa, M., Moumni, Z., Doaré, O., Touzé, C., Zaki, W., 2012. Non-linear dynamic thermomechanical behaviour of shape memory alloys. *J. Intell. Mater. Syst. Struct.* 23 (14), 1593–1611.
- Peng, H., Song, F., Wang, S., Zhang, C., Wen, Y., 2015. Role of carbon in improving the shape memory effect of Fe–Mn–Si–Cr–Ni alloys by thermo-mechanical treatments. *Smart Mater. Struct.* 24 (5), 055010.
- Rong, L., Ping, D., Li, Y., Shi, C., 1995. Improvement of shape memory effect in Fe–Mn–Si alloy by Cr and Ni addition. *Scr. Metall. Mater.* 32 (12), 1905–1909.
- Sato, A., Chishima, E., Soma, K., Mori, T., 1982. Shape memory effect in  $\gamma \rightleftharpoons \epsilon$  transformation in Fe–30Mn–1Si alloy single crystals. *Acta Metall.* 30 (6), 1177–1183.
- Sawaguchi, T., Kikuchi, T., Ogawa, K., Kajiwar, S., Ikeo, Y., Kojima, M., Ogawa, T., 2006. Development of prestressed concrete using Fe–Mn–Si-based shape memory alloys containing NbC. *Mater. Trans.* 47 (3), 580–583.
- Shabalovskaya, S.A., 1996. On the nature of the biocompatibility and on medical applications of NiTi shape memory and superelastic alloys. *Biomed. Mater. Eng.* 6 (4), 267–289.
- Simo, J., Kennedy, J., Govindjee, S., 1988. Non-smooth multisurface plasticity and viscoplasticity. loading/unloading conditions and numerical algorithms. *Int. J. Numer. Methods Eng.* 26 (10), 2161–2185.
- Siredey, N., Hautcoeur, A., Eberhardt, A., 2005. Lifetime of superelastic Cu–Al–Be single crystal wires under bending fatigue. *Mater. Sci. Eng.* 396 (1), 296–301.
- Stanford, N., Dunne, D.P., 2006. Thermo-mechanical processing and the shape memory effect in an Fe–Mn–Si-based shape memory alloy. *Mater. Sci. Eng.* 422 (1), 352–359.
- Stanford, N., Dunne, D.P., Li, H., 2008. Re-examination of the effect of NbC precipitation on shape memory in Fe–Mn–Si-based alloys. *Scr. Mater.* 58 (7), 583–586.
- Sutou, Y., Koeda, N., Omori, T., Kainuma, R., Ishida, K., 2009. Effects of ageing on bainitic and thermally induced martensitic transformations in ductile Cu–Al–Mn-based shape memory alloys. *Acta Mater.* 57 (19), 5748–5758.
- Sutou, Y., Omori, T., Kainuma, R., Ishida, K., 2013. Grain size dependence of pseudoelasticity in polycrystalline Cu–Al–Mn-based shape memory sheets. *Acta Mater.* 61 (10), 3842–3850.
- Tanaka, Y., Himuro, Y., Kainuma, R., Sutou, Y., Omori, T., Ishida, K., 2010. Ferrous polycrystalline shape-memory alloy showing huge superelasticity. *Science* 327 (5972), 1488–1490.
- Ueland, S.M., Schuh, C.A., 2012. Superelasticity and fatigue in oligocrystalline shape memory alloy microwires. *Acta Mater.* 60 (1), 282–292.
- Vincent, M., Thiebaud, F., Khalifa, S.B.H., Engels-Deutsch, M., Ben Zineb, T., 2015. Finite element analysis of a copper single crystal shape memory alloy-based endodontic instruments. *J. Mater. Eng. Perform.* 24 (10), 4128–4139.
- Wang, D., Chen, Y., Gong, F., Liu, D., Liu, W., 1995. The effect of thermomechanical training on the microstructures of Fe–Mn–Si shape memory alloy. *Le J. Physique IV* 5 (C8), C8–527.
- Watanabe, Y., Wakatsuki, T., Sato, H., Maruyama, T., 2007. Bending strength of Fe–Mn–Si–Cr shape memory alloy machining chips reinforced smart composite. *ICCM Int Conf Compos Mater.*
- Wen, Y., Xiong, L., Li, N., Zhang, W., 2008. Remarkable improvement of shape memory effect in an Fe–Mn–Si–Cr–Ni–C alloy through controlling precipitation direction of Cr<sub>23</sub>C<sub>6</sub>. *Mater. Sci. Eng.* 474 (1), 60–63.
- Wolf, E., 1970. Fatigue crack closure under cyclic tension. *Eng. Fract. Mech.* 2 (1), 37in345–44in4.
- Yamauchi, K., Ohkata, I., Tsuchiya, K., Miyazaki, S., 2011. *Shape memory and superelastic alloys: applications and technologies*. Elsevier.
- Zaki, W., 2010. An approach to modeling tensile–compressive asymmetry for martensitic shape memory alloys. *Smart Mater. Struct.* 19 (2), 025009.
- Zaki, W., 2012. Time integration of a model for martensite detwinning and reorientation under nonproportional loading using lagrange multipliers. *Int. J. Solids Struct.* 49 (21), 2951–2961.
- Zaki, W., Moumni, Z., 2007. A three-dimensional model of the thermomechanical behavior of shape memory alloys. *J. Mech. Phys. Solids* 55 (11), 2455–2490.
- Zaki, W., Moumni, Z., Morin, C., 2011. Modeling tensile-compressive asymmetry for superelastic shape memory alloys. *Mech. Adv. Mater. Struct.* 18 (7), 559–564.
- Zaki, W., Zamfir, S., Moumni, Z., 2010. An extension of the ZM model for shape memory alloys accounting for plastic deformation. *Mech. Mater.* 42 (3), 266–274.
- Zhao, C., 1999. Improvement of shape memory effect in Fe–Mn–Si–Cr–Ni alloys. *Metall. Mater. Trans. A* 30 (10), 2599–2604.